

# High and variable drag in a sinuous estuary with intermittent stratification

Tong Bo<sup>1</sup>, David Keith Ralston<sup>2</sup>, Wouter Michiel Kranenburg<sup>3</sup>, W Rockwell Geyer<sup>2</sup>, and Peter A. Traykovski<sup>4</sup>

<sup>1</sup>MIT, WHOI

<sup>2</sup>Woods Hole Oceanographic Institution

<sup>3</sup>Deltares

<sup>4</sup>WHOI

November 23, 2022

## Abstract

In field observations from a sinuous estuary, the drag coefficient  $C$ , much greater than expected from bottom friction alone.  $C$  are explained by form drag from flow separation at sharp channel bends. Greater water depths during flood tides corresponded with increased values of  $C_D$ , consistent with the expected depth dependence for flow separation, as flow separation becomes stronger in deeper water. Additionally, the strength of the adverse pressure gradient downstream of the bend apex, which is indicative of flow separation, correlated with  $C_D$  during flood tides. While  $C_D$  generally increased with water depth,  $C_D$  decreased for the highest water levels that corresponded with overbank flow. The decrease in  $C_D$  may be due to inhibition of flow separation with flow over the vegetated marsh. The dependence of  $C_D$  during ebbs on discharge corresponds with inhibition of flow separation by a favoring baroclinic pressure gradient that is locally generated at the bend apex due to curvature-induced secondary circulation. This effect increases with stratification, which increases with discharge. Additional factors may contribute to the high drag, including secondary circulation, multiple-scales of bedforms, and shallow shoals, but the observations suggest that flow separation is the primary source.

# High and variable drag in a sinuous estuary with intermittent stratification

Tong Bo<sup>1,2,\*</sup>, David K. Ralston<sup>1</sup>, Wouter M. Kranenburg<sup>1,3</sup>, W. Rockwell Geyer<sup>1</sup>, and Peter Traykovski<sup>1</sup>

<sup>1</sup>Woods Hole Oceanographic Institution, Applied Ocean Physics and Engineering, Woods Hole, MA 02543, United States

<sup>2</sup>MIT-WHOI Joint Program, Cambridge, MA 02139, United States

<sup>3</sup>Deltares, Marine and Coastal Systems, PO box 177, 2600MH, Delft, The Netherlands

\*Corresponding author: Tong Bo, tongbo@mit.edu

March 2, 2021

## Key Points:

- The drag in a sinuous estuary is greater than expected from bottom friction alone, and it varies at tidal and seasonal time scales.
- Form drag due to flow separation at sharp bends can explain the high drag and its tidal asymmetry.
- Overbank flow and stratification may inhibit flow separation and decrease the associated form drag.

## Abstract

In field observations from a sinuous estuary, the drag coefficient  $C_D$  based on the momentum balance was in the range of  $5 - 20 \times 10^{-3}$ , much greater than expected from bottom friction alone.  $C_D$  also varied at tidal and seasonal time scales.  $C_D$  was greater during flood tides than ebbs, most notably during spring tides. The ebb tide  $C_D$  was negatively correlated with river discharge, while the flood tide  $C_D$  showed no dependence on discharge. The large values of  $C_D$  are explained by form drag from flow separation at sharp channel bends. Greater water depths during flood tides corresponded with increased values of  $C_D$ , consistent with the expected depth dependence for flow separation, as flow separation becomes stronger in deeper water. Additionally, the strength of the adverse pressure gradient downstream of the bend apex, which is indicative of flow separation, correlated with  $C_D$  during flood tides. While  $C_D$  generally increased with water depth,  $C_D$  decreased for the highest water levels that corresponded with overbank flow. The decrease in  $C_D$  may be due to inhibition of flow separation with flow over the vegetated marsh. The dependence of  $C_D$  during ebbs on discharge corresponds with inhibition of flow separation by a favoring baroclinic pressure gradient that is locally generated at the bend

14 apex due to curvature-induced secondary circulation. This effect increases with stratification, which increases  
15 with discharge. Additional factors may contribute to the high drag, including secondary circulation, multiple-  
16 scales of bedforms, and shallow shoals, but the observations suggest that flow separation is the primary source.

17 **Plain Language Summary** In shallow estuaries, bottom roughness is usually a major contribution to the flow  
18 resistance. The drag coefficient  $C_D$  is a dimensionless number that is typically used to quantify the overall flow  
19 resistance. In field observations from a sinuous estuary,  $C_D$  was much greater than expected from bottom roughness  
20 alone. We find that sharp bends in the channel lead to flow separation and recirculating eddies, and this creates  
21 "form drag" that removes energy from the flow. Our analysis links the increased  $C_D$  to evidence of flow separation,  
22 and also explains tidal and seasonal variations in  $C_D$ . This observational study suggests that channel curvature can  
23 greatly increase flow resistance and affect the tidal dynamics in similar estuaries.

## 24 **1 Introduction**

25 The drag force is an important part of the estuarine momentum balance, and it directly affects tidal propagation,  
26 flooding potential, and marsh inundation, as well as estuarine exchange, mixing processes and salinity intrusion  
27 (e.g., Geyer, 2010). Models to predict water level elevations and velocities in estuaries require appropriate parame-  
28 terization of the drag (e.g., Lewis and Lewis, 1987). The drag coefficient  $C_D$  is one of the typical ways to quantify  
29 the drag and is defined as

$$C_D = \frac{\tau}{\rho U |U|}, \quad (1)$$

30 where  $\tau$  is the total drag,  $\rho$  is density, and  $U$  is a reference velocity, usually taken at a fixed elevation (e.g., 1 m  
31 above the bed) or as the depth average.

32 Drag in shallow flows (e.g., estuaries, rivers, and the coastal ocean) is mainly attributed to bottom friction. A  
33 common value for  $C_D$  used in estuaries and tidal channels is around  $3 \times 10^{-3}$  (e.g., Dronkers, 1964; Sternberg,  
34 1968; Soulsby, 1990; Geyer et al., 2000), but  $C_D$  can vary depending on the dominant sources of drag.  $C_D$  due  
35 to bottom roughness can be calculated directly by assuming a near-bed boundary layer velocity profile (e.g., Gross  
36 et al., 1999; Lentz et al., 2017). The bottom friction also depends on the size and structure of roughness elements  
37 like bed forms (Grant and Madsen, 1982; Fong et al., 2009) and can be enhanced by wind waves (Grant and  
38 Madsen, 1986; Bricker et al., 2005). Factors other than bottom friction can also contribute to the drag, e.g., stem  
39 drag from vegetation (e.g., Kadlec, 1990; Nepf, 1999) and form drag from large topographic features including  
40 headlands (McCabe et al., 2006) and channel bends (Seim et al., 2006).

41 A sinuous channel planform is a common feature of many estuaries (Marani et al., 2002) and the channel  
42 curvature influences the flow structure and the drag (e.g., Leeder and Bridges, 1975; Lacy and Monismith, 2001;  
43 Chant, 2002; Seim et al., 2006). Increased flow resistance due to channel curvature has been examined extensively  
44 in rivers and laboratory channels (e.g., Chow, 1959; Leopold, 1960; Chang, 1984; Arcement and Schneider, 1989).  
45 Several processes have been identified as contributing to increased drag in sinuous channels, including secondary  
46 circulation (e.g., Chang, 1984) and flow separation (e.g., Leopold, 1960).

47 Secondary circulation due to flow curvature interacts with the primary along-channel flow to increase drag.  
48 Flow around a bend generates a water level setup near the outer bank and a setdown near the inner bank (Thomson,  
49 1877; Kalkwijk and Booij, 1986). This lateral water level slope yields a barotropic pressure gradient that balances  
50 the centrifugal acceleration. Vertical shear in the streamwise flow causes a depth-dependent imbalance between  
51 these two forcing terms and, as a result, secondary circulation develops in the lateral plane perpendicular to the pri-  
52 mary flow direction. In estuaries, lateral baroclinic pressure gradients caused by salinity variation can also affect the

53 secondary circulation in bends (e.g., Nidzieko et al., 2009; Kranenburg et al., 2019). Laboratory experiments have  
54 shown that secondary circulation can increase drag by: (1) increasing the lateral velocity and creating an additional  
55 bed shear stress component; (2) vertically advecting high momentum toward the channel bed, compressing the bot-  
56 tom boundary layer, and increasing the bottom stress (Chang, 1983; Blanckaert and de Vriend, 2003; Blanckaert  
57 and Graf, 2004). In observations from estuaries, secondary circulation associated with channel curvature has been  
58 found to increase turbulent stresses and the drag (Seim et al., 2002; Fong et al., 2009).

59 In addition to secondary circulation, drag can be enhanced due to flow separation and the associated form drag  
60 at channel bends. Channel curvature creates a lateral water level slope in the bend, and as the curvature effect  
61 decreases downstream from the bend apex, the lateral water level slope decreases toward the exit of the bend. As a  
62 result, an adverse pressure gradient can occur along the inner bank, potentially causing flow separation (Blanckaert,  
63 2010; Vermeulen et al., 2015). With flow separation, streamlines of the main flow detach from the inner bank and  
64 recirculating lee eddies are generated (Leopold, 1960; Leeder and Bridges, 1975). The separation zone has a lower  
65 water surface elevation than the main flow, and the resulting pressure difference around the bend creates form drag  
66 that can be a major contribution to the total drag (McCabe et al., 2006; Bo and Ralston, 2020). The drag associated  
67 with flow separation have been studied in laboratory experiments with unidirectional flow (e.g., Leopold, 1960;  
68 James et al., 2001), and Bo and Ralston (2020) conducted numerical model studies to investigate form drag and  
69 explain its parameter dependence in curved estuarine flows with idealized channels.

70 In this research we calculate from observations the drag coefficient in an estuary with channel curvature and  
71 intermittent stratification, and investigate factors potentially contributing to the observed drag coefficients that  
72 are greater than expected from bottom roughness alone. In section 2, we introduce the field site, measurements,  
73 and data processing methods. The calculated drag coefficient and its dependence on tides and river discharge  
74 are shown in section 3. In section 4, we examine factors contributing to the increased drag, including evidence  
75 of flow separation and form drag at bends, dependence on overbank flow, and the influence of stratification. In  
76 section 5, we explain the increased drag and its variability, and discuss other potential contributors. Section 6  
77 presents conclusions.

## 78 **2 Methods**

### 79 **2.1 Field site**

80 The field study was conducted in the North River estuary (Massachusetts, USA), a narrow, sinuous channel through  
81 a salt marsh (Figure 1 (a)). The tidal range of the North River varies between 2 m and 3.5 m. Intertidal marshes

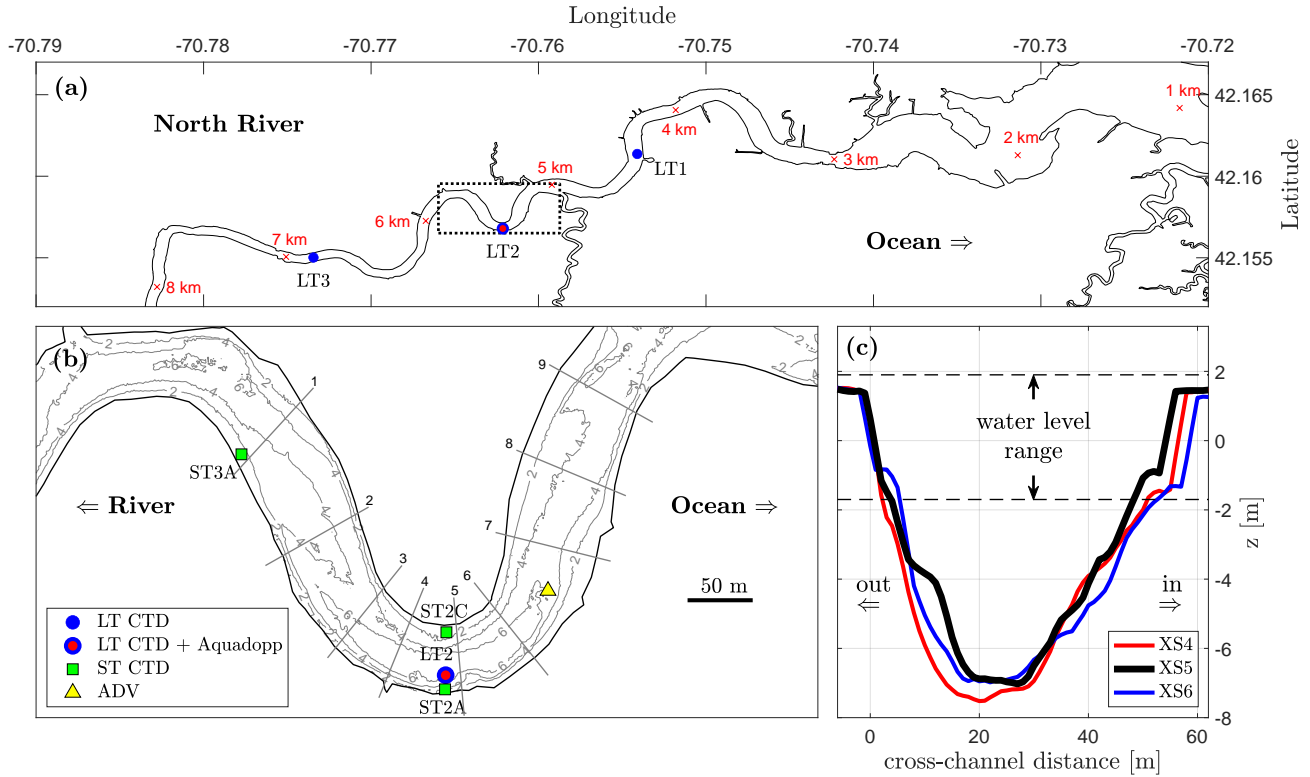


Figure 1: **(a)**: The North River estuary, with the intensive study area marked by the rectangle. Red crosses mark the along-channel distance from the mouth. **(b)**: The intensive study area with contours showing the bathymetry, with locations of long-term (LT) CTDs, short-term (ST) CTDs, Aquadopp profiler, and ADV measurements. Gray lines represent shipboard survey transects. **(c)**: Three cross-sectional profiles near the bend apex that correspond to transects 4, 5, 6 in **(b)**. The two dashed lines show the tidal water level range and  $z = 0$  is the mean water level.

82 are widespread over the banks and are inundated during high spring tides. The North River has a modest discharge,  
 83 based on USGS discharge measurements in a contributory stream upriver (station 01105730) that have been scaled  
 84 up according to the total catchment area (Kranenburg et al., 2019). During the high-flow season of the spring, the  
 85 discharge is typically  $5 - 10 \text{ m}^3/\text{s}$  (corresponding to a mean velocity of  $2 - 4 \text{ cm/s}$  in the mid-estuary) with increases  
 86 of up to  $30 \text{ m}^3/\text{s}$  for rain-event peaks. In the low-flow season of summer, discharge is typically less than  $5 \text{ m}^3/\text{s}$ .  
 87 The North River estuary is intermittently stratified, with seasonal variation that is examined in section 3.1.

88 The focus of this study is in the mid-estuary, centered around a sharp bend at about 5.4 km from the mouth  
 89 of the estuary. The mid-estuary channel has a typical width  $W$  of about 50 m and average depth  $H$  of about 5 m,  
 90 i.e., an aspect ratio  $W/H \approx 10$ , which is common for salt marsh meanders (Marani et al., 2002). At the apex of  
 91 the sharp bend that was the focus of the observations, the radius of curvature is  $R \approx 60 \text{ m}$ , yielding a curvature  
 92 ratio  $R/W \approx 1.2$ . Most other mid-estuary bends are less sharp, with a radius of curvature of around  $100 - 200 \text{ m}$   
 93 and  $R/W$  of  $2 - 4$ . The range of  $R/W$  in the North River is representative of the bend sharpness generally found  
 94 in sinuous rivers (Leopold and Wolman, 1960) and tidal channels (Marani et al., 2002), where  $R/W$  values are

95 typically in the range of 1.5 – 5 and sharp bends can have  $R/W$  of around 1 (e.g., Nanson, 2010; Schnauder  
96 and Sukhodolov, 2012; Marani et al., 2002). The cross-sectional profile at the sharp bend apex is approximately  
97 symmetric laterally, with relatively steep banks and no distinct point bar (Figure 1 (c)). Shallow shoals exist along  
98 the inner bank on the seaward side of the sharp bend, and also on the seaward side of the inner bank of the next  
99 bend landward.

100 Kranenburg et al. (2019) investigated the lateral circulation patterns at the apex of the sharp bend. The “normal”  
101 helical circulation for flow around a bend was observed during ebb tide, with inward flow near the bottom and  
102 outward flow near the surface. However, during flood tide, lateral circulation was reversed from the “normal”  
103 structure, with flow toward the inner bank near the surface and toward the outer bank in the lower layer. During  
104 both flood and ebb, streamwise velocity was greatest near the inner bank, which is consistent with potential flow  
105 due to curvature and indicates that friction does not play as big a role in shifting the velocity maximum toward  
106 the outer bank as is found in many river and laboratory meanders (e.g., Jamieson et al., 2013; Blanckaert, 2015).  
107 The lateral shear in the streamwise velocity creates lateral salinity differences through differential advection of the  
108 along-estuary salinity gradient. During ebbs the lateral baroclinic pressure gradient reinforces the “normal” lateral  
109 circulation, but during flood tides the lateral baroclinic forcing is outward and counteracts the inward barotropic  
110 pressure gradient (Kranenburg et al., 2019). Triggered by this lateral baroclinic forcing, the sense of secondary  
111 circulation can therefore be reversed during flood tide.

## 112 **2.2 Measurements**

113 The field measurements used in this study overlap with those from Kranenburg et al. (2019), including time series  
114 of velocity, pressure and salinity from April 4 to July 31 in 2017 (long-term (LT) moorings). Pressure and salinity  
115 were measured at three mooring locations by conductivity-temperature-depth (CTD) sensors sampled every 2 min:  
116 one mooring at the bend apex (LT2) and two at comparable distances down-estuary (LT1) and up-estuary (LT3) of  
117 the bend, i.e., 4.4, 5.4 and 6.9 km from the mouth respectively (Figure 1 (a)). Five CT(D) sensors were deployed  
118 at LT2 with similar vertical spacing through the water column, and two CT(D) sensors were deployed near the  
119 surface and bed at each of LT1 and LT3. Velocity profile data were collected at the bend apex (same location as  
120 the LT2 CTD, about 15 m from the outer bank, Figure 1) by an upward-looking Aquadopp profiler (0.2-m vertical  
121 resolution, 10-min sample interval, 45-s averaging period) mounted on a bottom frame. In addition, short-term  
122 (ST) CTD sensors were deployed at the inner (ST2C) and outer (ST2A) bank of the bend apex and at the south  
123 side of the up-estuary exit of the bend (ST3A) from April 18 to May 24 (Figure 1 (b)). Short-term CTDs were also  
124 deployed near the inner bank landward of the bend and near both banks seaward of the bend, but these deployments

125 failed. Shipboard surveys were conducted on April 18, 19, and 27, May 17, and July 24, 25, 28, and 31 with an  
 126 acoustic Doppler current profiler (ADCP, cell size 0.50 m, profile interval 0.25 s) over cross-sections 1 – 9 through  
 127 the bend and temperature-salinity profile measurements at lateral cross-sections 1, 3, 5, 7 and 9 (Figure 1 (b)). An  
 128 acoustic Doppler velocimeter (ADV) was deployed near the bend apex (Figure 1 (b)) from July 24 to July 27 in  
 129 2017 for high-frequency velocity measurement (16-Hz sample rate, 12-min bursts) at about 0.5 m above the bed.

130 Bathymetric surveys of the study site were conducted using a Jetyak Unmanned Surface Vehicle (Kimball et al.,  
 131 2014). The Jetyak was equipped with a bathymetric sidescan sonar, and a post-processing kinematic global navi-  
 132 gation system sensor coupled to a inertial motion sensor for attitude heading reference and position measurements.  
 133 The bathymetric sonar is optimized for shallow water surveys, and is capable of measuring seafloor topography  
 134 with resolution and accuracy of better than 10 cm in both lateral and vertical dimensions in swath widths of up to  
 135 10 times the water depth. The final bathymetric output was gridded in 50-cm bins for overall bathymetry of the the  
 136 mid-estuary region (Figure 1), and selected areas were gridded at 20 cm for detailed analysis of bedform geometry.

## 137 **2.3 Data analysis**

138 We calculated the drag in the North River estuary using multiple approaches. First, the drag coefficient  $C_D$  was  
 139 calculated from the depth-averaged along-estuary momentum balance, and it represents the total momentum loss  
 140 in the observation region. The along-estuary momentum balance includes the along-estuary time-mean water level  
 141 gradient, which is not measured directly but is estimated from theory and forcing conditions. In addition, we  
 142 estimated the drag coefficient  $C_{D,energy}$  using the tidal energy flux balance since drag causes energy dissipation.  
 143 In addition to these larger-scale estimates of the total drag, the bottom friction coefficient  $C_f$  was calculated from  
 144 local high-frequency velocity measurements and reflects the near-bed shear stress.

### 145 **2.3.1 Drag coefficient from the momentum balance**

146 An approximate depth-averaged along-estuary momentum equation is

$$\frac{\partial U}{\partial t} = -g \frac{\partial \eta}{\partial s} - \frac{1}{2} \beta g \frac{\partial \langle S \rangle}{\partial s} H - \frac{C_D U |U|}{H}, \quad (2)$$

147 where we have neglected the advection and Coriolis terms. While advection can be a significant contributor to the  
 148 local momentum balance in the bends, the advection term is less important when assessing the momentum budget  
 149 at larger scales.  $\eta$  is the water level,  $\langle S \rangle$  is the depth-averaged salinity and  $H$  is the water depth.  $s$  is the along-  
 150 channel coordinate and  $\beta$  is the haline contraction coefficient.  $C_D$  is the drag coefficient used to represent the total

151 flow resistance including bottom friction and other sources of drag. In this analysis,  $C_D$  is defined based on the  
152 depth averaged streamwise velocity  $U$ .

153 We can therefore calculate a drag coefficient that satisfies the momentum budget in the North River estuary  
154 using

$$C_D = \left( \frac{\partial U}{\partial t} + g \frac{\partial \eta}{\partial s} + \frac{1}{2} \beta g \frac{\partial \langle S \rangle}{\partial s} H \right) / \left( \frac{-U|U|}{H} \right). \quad (3)$$

155  $U$  was measured by the Aquadopp profiler at the bend apex, and calculated as the vertical average of the velocity  
156 profile. The velocity has been extrapolated in the near-bed (0.4 m) and near-surface ( $\sim 0.8$  m) regions that are  
157 not covered by Aquadopp measurements due to the mount height, blanking distance, and surface interference.  
158 The tidal water level gradient and salinity gradient were calculated using LT1 and LT3 CTD measurements down-  
159 and up-estuary of the bend based on centered difference. In addition, the measured tidal water level gradient was  
160 adjusted to account for the time-mean along-estuary water level gradient that could not be assessed directly with the  
161 measurements (further explained in section 2.3.2).  $H$  is the laterally averaged water depth, with the time series of  
162 the single-location water depth recorded by the LT2 CTD at the apex and converted to a lateral average using data  
163 from shipboard cross-channel surveys. Average depth  $H$  is calculated for the channel width, and does not include  
164 the marsh extent for periods with overbank flow. The lateral average is used because any single location cannot  
165 represent the nonuniform cross-channel bathymetry, and depth is a key variable in the stress divergence term.

166 The velocity data was based on a single location measurement near the outer bank, but the depth-averaged  
167 velocity also can have lateral variability. Therefore, the Aquadopp data was compared with the cross-sectional  
168 average velocity from ADCP surveys near the mooring. Based on comparison of ten tides, the ratio of the moored  
169 velocity measurement to the cross-sectional average had a mean value of 1 for both flood and ebb tides, with  
170 variations of less than 10%. The ADCP surveys do not indicate bias in the Aquadopp data compared with the  
171 cross-channel average, so the depth-averaged velocity from the mooring is used in the calculation of  $C_D$ . The  
172 Aquadopp mooring site was near the bend apex, and the lateral structure of the depth and velocity also varies  
173 through the bend. ADCP and bathymetry surveys of multiple transects along the bend were compared with the  
174 transect at the bend apex. The apex transect had a greater average depth than other transects, and higher velocity  
175 due to channel convergence. The calculated  $U|U|/H$  at the apex transect, representing the stress divergence term  
176 in (2), was similar to the average  $U|U|/H$  at other transects in the bend.

177 The drag term is quadratic with velocity and velocity is in the denominator of (3), and therefore we focus on  
178 the averaged  $C_D$  over 1-hr windows around maximum flood and ebb tide to reduce the sensitivity to low velocity  
179 periods. The calculated  $C_D$  applies to the total momentum loss at the scale of the spacing between the pressure

180 sensors ( $\sim 2.5$  km) in the mid-estuary region that contains the sharp studied bend as well as several other bends  
 181 that are less sharp.

### 182 2.3.2 Mean along-estuary barotropic pressure gradient

183 The measured instantaneous water level at each location is the free surface deviation from the local mean water  
 184 level, i.e.,  $\eta' = h - \bar{h}$ , where  $h$  is the instantaneous depth measured by CTD sensors and  $\bar{h}$  is the time-mean depth.  
 185 The time-mean depth is calculated using a low-pass filter over 33 hours to allow for longer term variation in the  
 186 measurements that do not reflect the tidal dynamics (e.g., instrument drift or movement). The measured water  
 187 levels are not referenced to an absolute vertical coordinate, and to obtain the absolute water level, the measured  
 188 instantaneous water level  $\eta'$  must be corrected as

$$\eta = \eta' + \bar{\eta}, \quad (4)$$

189 where  $\eta$  is the absolute water level and  $\bar{\eta}$  is the time-mean water level (varying at subtidal time-scale) that was  
 190 not directly resolved in the North River observations. The calculation of  $C_D$  was based on measurements of the  
 191 instantaneous water level gradient in the along-estuary momentum balance, with the absolute water level gradient  
 192 forcing being

$$g \frac{\partial \eta}{\partial s} = g \frac{\partial \eta'}{\partial s} + g \frac{\partial \bar{\eta}}{\partial s}. \quad (5)$$

193 The first term on the right side is the measured water level gradient forcing calculated between LT1 and LT3  
 194 CTDs. The second term is the unresolved time-varying mean (subtidal) water level gradient forcing that needs to  
 195 be incorporated into the momentum balance.

196 A mean along-estuary water level gradient can be generated due to river inputs or by tidal processes, and is typ-  
 197 ically a water level setup from seaward to landward. In the mean along-estuary momentum balance, the mean water  
 198 level gradient forcing (barotropic pressure gradient, BTPG) is balanced with three forcing terms (Appendix A): the  
 199 bottom friction from the mean flow, the tidal stress (e.g., Nihoul and Roday, 1975), and the mean salinity gradient  
 200 forcing (baroclinic pressure gradient, BCPG).

201 The bottom friction from the mean flow is estimated as (e.g., Nihoul and Roday, 1975; Parker, 2007)

$$\tau_{b,\bar{u}} = -\frac{4}{\pi} C_f \rho \|U\| \bar{U}, \quad (6)$$

202 where  $C_f$  is the bottom friction coefficient,  $\|U\|$  is the norm of tidal velocity, i.e., the amplitude of the periodic

203 velocity, and  $\bar{U}$  is the mean flow or residual current.  $\bar{U}$  is typically seaward in the estuary, and is dominated by  
 204 the freshwater discharge but also includes the Eulerian return flow of the landward Stokes drift of the tidal forcing  
 205 (Zimmerman, 1979; Uncles and Jordan, 1980).  $\bar{U}$  and  $\|U\|$  were calculated from the depth averaged velocity  
 206 measurements by the LT Aquadopp profiler at the bend apex (section 2.2).  $C_f$  was set as  $3 \times 10^{-3}$ , a typical value  
 207 for bottom friction that is consistent with the ADV measurements (section 3.3).

208 The tidal stress is estimated as (e.g., Nihoul and Ronday, 1975; Zimmerman, 1978)

$$\tau_t = -\frac{1}{4}\rho g \frac{\partial}{\partial s} (\|\eta\|^2), \quad (7)$$

209 where  $\|\eta\|$  is the norm of tidal water level fluctuation, i.e., tidal amplitude. Details of the derivation are in Ap-  
 210 pendix A.  $\tau_t$  is a manifestation of the radiation stress in a tidal wave (Zimmerman, 1978) and is in the direction of  
 211 tidal amplitude decay. The tidal amplitude decay was calculated between the down-estuary (LT1) and up-estuary  
 212 (LT3) moorings.

213 The mean depth-averaged BCPG (salinity gradient forcing) was calculated using

$$\text{mean BCPG} = -\frac{1}{2}\beta g \frac{\partial \langle S \rangle}{\partial s} H, \quad (8)$$

214 where the salinity gradient was estimated between LT1 and LT3 CTDs and the overbar means time averaged (low-  
 215 pass filtered results).

216 We can estimate the mean BTPG on the North River estuary from the mean momentum balance by calculating  
 217 the mean flow bottom friction, the tidal stress, and the mean BCPG, i.e.,

$$g \frac{\partial \bar{\eta}}{\partial s} = \frac{1}{\rho H} (\tau_{b,\bar{u}} + \tau_t) - \frac{1}{2}\beta g \frac{\partial \langle S \rangle}{\partial s} H, \quad (9)$$

218 where  $\bar{H}$  is the mean water depth (low-pass filtered  $H$  measured by the LT2 CTD). The absolute BTPG can  
 219 therefore be calculated by substituting in (9) into (5)

$$g \frac{\partial \eta}{\partial s} = g \frac{\partial \eta'}{\partial s} + \frac{1}{\rho H} (\tau_{b,\bar{u}} + \tau_t) - \frac{1}{2}\beta g \frac{\partial \langle S \rangle}{\partial s} H. \quad (10)$$

220 **2.3.3 Drag coefficient from the energy flux balance**

221 The second method to calculate the drag is based on the tidal energy budget. The energy flux balance for the  
 222 depth-integrated tidal flow is (van Rijn, 2011)

$$\frac{\partial \|\eta\|}{\partial s} = 0.5(\gamma_w + \gamma_h)\|\eta\| - \frac{4C_D\|U\|^2}{3\pi g\bar{H}\cos(\Delta\phi)}, \quad (11)$$

223 where  $\|\eta\|$  is tidal amplitude and  $\|U\|$  is the amplitude of tidal velocity.  $\Delta\phi$  is the phase difference between tidal  
 224 water level and velocity.  $\gamma_w$  and  $\gamma_h$  are the convergence coefficients for channel width and depth.

$$\gamma_w = \frac{1}{L_w}, \quad \gamma_h = \frac{1}{L_h}, \quad (12)$$

225 with  $L_w$  and  $L_h$  being the e-folding scales for channel width and depth change. The channel depth convergence  
 226 rate  $\gamma_h$  is set to be zero ( $L_h = \infty$ ), because there is no clear trend in channel depth in the mid-estuary region.  
 227 The channel width has an overall landward decreasing trend, although local variations exist with expansions and  
 228 convergences of  $O(100\text{ m})$ . Exponential fitting to the channel width yields an  $L_w \approx 20\text{ km}$ .

229 We can calculate the drag coefficient by rearranging (11),

$$C_{D,energy} = \left( -\frac{\partial \|\eta\|}{\partial s} + 0.5(\gamma_w + \gamma_h)\|\eta\| \right) \frac{3\pi g\bar{H}\cos(\Delta\phi)}{4\|U\|^2}. \quad (13)$$

230 The tidal energy flux balance (13) provides a method to calculate the drag coefficient different from (3), as  
 231  $C_{D,energy}$  represents the tidal energy loss due to drag. Tidal analysis was applied to the water level data col-  
 232 lected by the three LT CTDs and the velocity  $U$  measured by the Aquadopp profiler at bend apex, with an analysis  
 233 window length of 99 hours (eight M2 tidal cycles). Tidal amplitude  $\|\eta\|$  was calculated from the LT2 CTD data,  
 234  $\|U\|$  was from the Aquadopp profiler collocated with the LT2 CTD, and  $\Delta\phi$  is their phase difference. The tidal  
 235 amplitude gradient was calculated between the LT1 and LT3 CTDs.

236 **2.3.4 Bottom friction coefficient**

237 The local near-bed shear stress was calculated from the high frequency ADV measurements near the bend apex.  
 238 The bottom shear stress is quantified by the bottom friction coefficient  $C_f$  (similar to  $C_D$ , but only quantifies  
 239 bottom stress), estimated using (e.g., Bowden and Fairbairn, 1956)

$$C_f = \frac{\overline{u'w'}}{\bar{u}^2} = \frac{\int S_{uw}dk}{\bar{u}^2}. \quad (14)$$

240  $\bar{u}$  is the burst-averaged streamwise velocity.  $u'$  and  $w'$  are the temporal fluctuations of streamwise and vertical  
 241 velocity around their means;  $\overline{u'w'}$  is the Reynolds stress;  $S_{uw}$  is the wave number cospectrum of  $u'$  and  $w'$ .

242 Additionally, the  $C_f$  has been calculated from the near-bed dissipation rate  $\epsilon$  (e.g., Kaimal et al., 1972) using  
 243 law of the wall scaling

$$\epsilon = \frac{u_*^3}{\kappa z_a}, \quad (15)$$

244 where  $u_* = \sqrt{\tau_b/\rho}$  is the shear velocity and  $\tau_b$  is the bottom shear stress.  $\kappa = 0.41$  is the von Kármán constant  
 245 and  $z_a = 0.5$  m is the height of ADV above the bed. Therefore,

$$C_f = \frac{u_*^2}{\bar{u}^2} = \frac{(\kappa z_a \epsilon)^{2/3}}{\bar{u}^2} \quad (16)$$

246 by substituting (15).  $\epsilon$  is estimated from the wave number spectrum of  $w'$

$$S_{ww}(k) = a_0 \epsilon^{2/3} k^{-5/3} \quad (17)$$

247 with  $a_0 = 0.68$  (e.g., Tennekes et al., 1972).

## 248 **3 Results**

### 249 **3.1 Estuarine conditions**

250 The laterally averaged water depth at the bend apex in the North River estuary ranges between 2 m and 5.5 m as a  
 251 result of tidal water level variation (Figure 2 (a)), with the tidal range varying between 2 m and 3.5 m from neap to  
 252 spring tides. The water level is higher during flood tide than during ebb tide due to the phase difference between  
 253 water level and velocity being less than 90 degrees (examined below). The tides are dominated by the semi-diurnal  
 254 M2 tide (1.2-m amplitude), with contributions from the S2 constituent (0.1 m), N2 constituent (0.3 m), and the  
 255 diurnal K1 constituent (0.1 m). Stronger and weaker spring-neap tides appear each lunar month due to the N2 tidal  
 256 constituent. During the observation period, the stronger spring tides occur around the end of each month. At the  
 257 mooring locations, the tidal amplitude ranges between 0.9 m and 1.5 m with increasing phase lag from LT1 to LT3  
 258 (Figure 3 (a)). The tidal amplitude is similar between LT1 and LT2, and decreases at LT3. Note that the analysis  
 259 used a 99-hr low-pass filter window, so the calculated tidal amplitude may be slightly different from the range of  
 260 fluctuations in the original water depth record. The tidal velocity amplitude varies between 0.35 m/s and 0.55 m/s  
 261 and the velocity phase leads that of the water level by 45 (spring tides) to 55 (neap tides) degrees, so the tidal wave

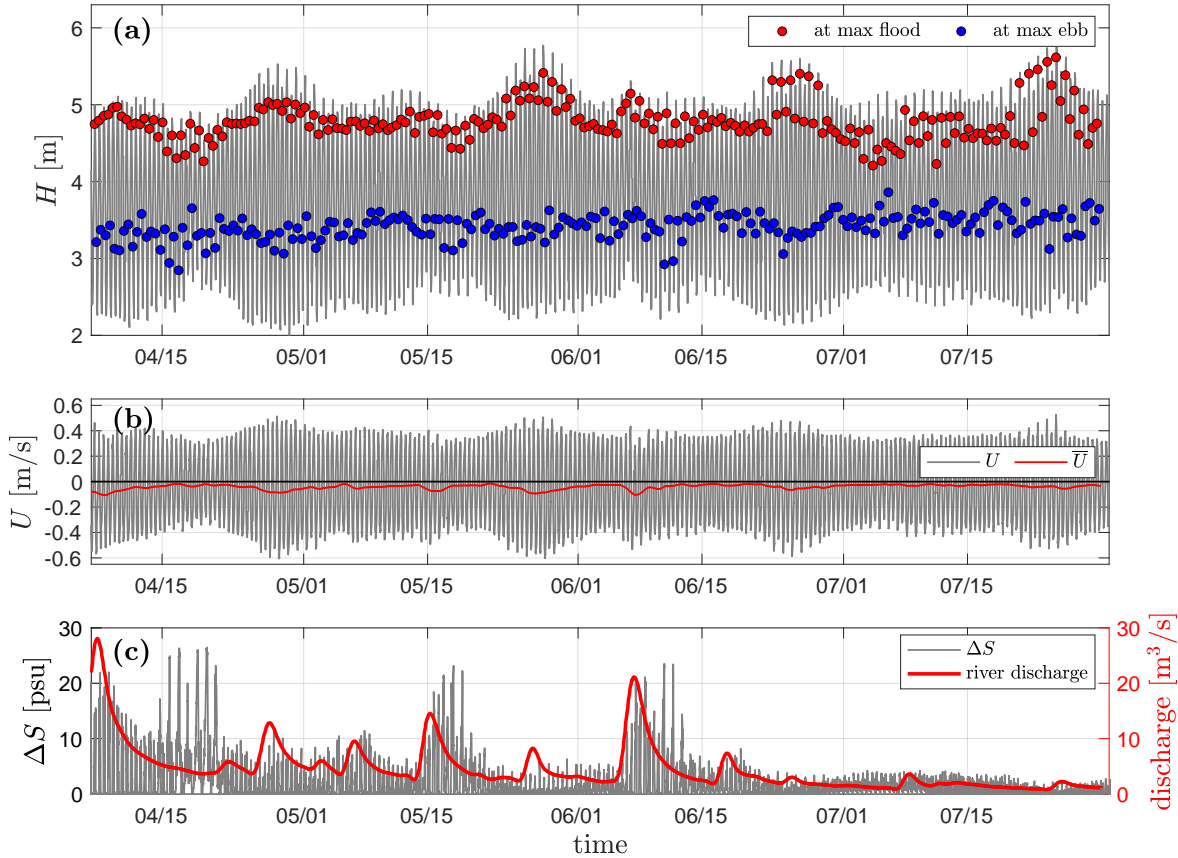


Figure 2: **(a)**: Water depth at the bend apex in the North River estuary. Red dots represent water depth at max flood tide; blue dots at max ebb tide. **(b)**: Black line: depth-averaged velocity at the bend apex; red line: low-pass filtered (33 hr) velocity.  $U > 0$  is flood tide. **(c)**: Left axis: stratification (surface-to-bottom salinity difference) at the bend apex; right axis: river discharge.

262 is partially progressive (Figure 3 **(b)**).

263 Stratification is calculated as the surface-to-bottom salinity difference  $\Delta S$  (Figure 2 **(c)**). Stratification is  
 264 stronger early in the observation period (before mid-June) due to the greater freshwater discharge. The greatest  
 265 stratification (e.g.,  $\Delta S > 10$  psu) is found during high discharge events or neap tides. Tidally, stratification is most  
 266 common from max flood tide through late flood and early ebb tide, and  $\Delta S$  is less than 1 psu at max ebb tide except  
 267 for during the weakest neap tides (less than 10% of the data record). Stratification is weaker in the summer (after  
 268 mid-June) when freshwater discharge is less, with peaks of  $\Delta S \sim 1 - 5$  psu during early flood and ebb tides and  
 269  $\Delta S < 1$  psu most of the rest of the tidal cycle. Therefore we describe the North River estuary as intermittently  
 270 stratified.

271 The time-mean BTPG on the North River estuary was estimated using the mean momentum balance (9) by  
 272 calculating the tidal stress, the mean flow bottom friction, and the mean BCPG (Figure 3 **(c)**). The mean flow  
 273 friction increases during high discharge periods or high spring tides when a stronger mean current is generated due

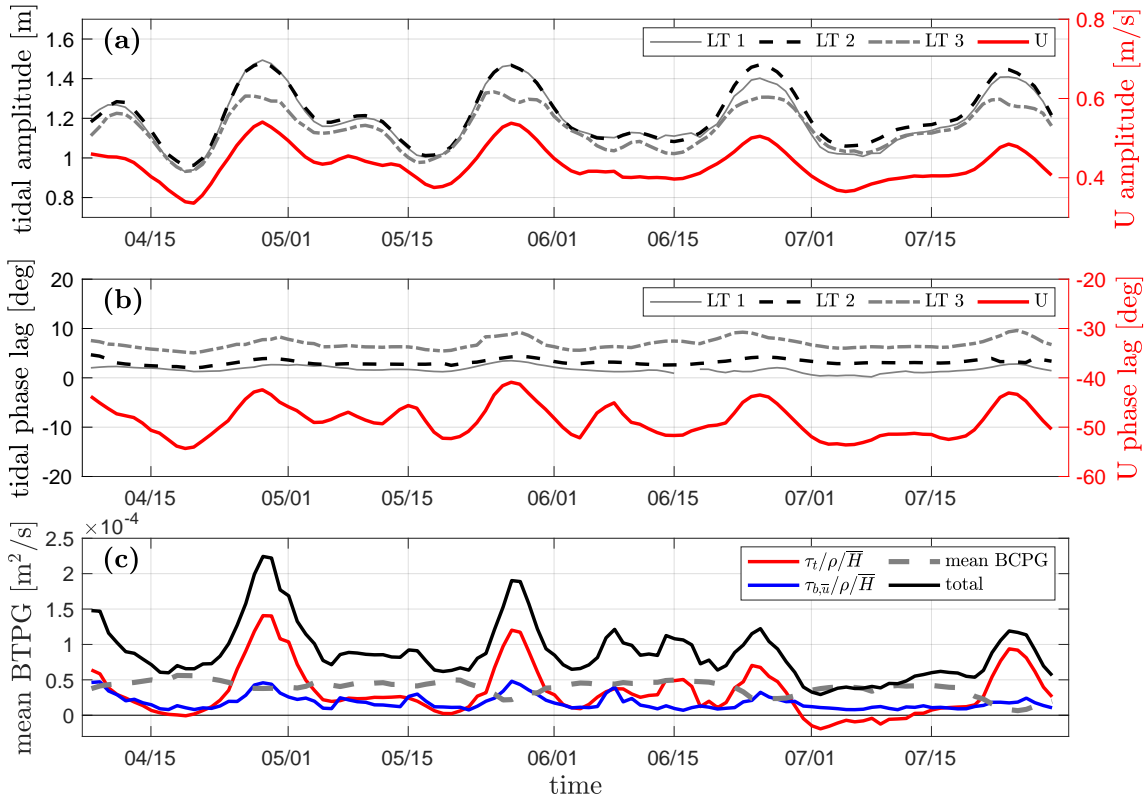


Figure 3: **(a)**: Left axis: tidal amplitude at LT1, LT2, and LT3; right axis: velocity amplitude at LT2. **(b)**: Left axis: tidal phase lag at LT1, LT2, and LT3, referenced to the tidal phase near the estuary mouth; right axis: velocity phase lag at LT2. Note the difference in vertical axis range. **(c)**: Terms that contribute to the mean along-channel BTPG. The red line represents the tidal stress; the blue line represents the mean bottom friction; the dashed gray line represents the mean BCPG; the black line is the total of the above three terms that is balanced by the mean BTPG.

274 to greater Stokes drift (e.g., Uncles and Jordan, 1980); the tidal stress increases during high spring tides because  
 275 tidal decay is more rapid when tidal forcing is stronger (Appendix A); the mean BCPG decreases during high spring  
 276 tides because of the greater salinity intrusion length. The three terms have similar magnitudes, but the tidal stress  
 277 is more sensitive to tidal forcing and can be dominant during high spring tides. The time-mean BTPG calculated  
 278 from these three terms is large during large spring tides (e.g., in late April, May, June, and July) and during several  
 279 high discharge events (e.g., in early April and early June). The seaward mean flow results in a landward bottom  
 280 friction. The tidal stress is in the direction of decreasing tidal amplitude, so it is mostly landward in this shallow and  
 281 weakly-converging estuary, except in early July when the tidal stress becomes seaward because the tidal amplitude  
 282 is larger at mooring site LT3 than LT1 (Figure 3 (a)). The mean BCPG has a landward forcing because salinity  
 283 decreases from seaward to landward. The mean BTPG balances these three terms, and always provides a seaward  
 284 forcing during the observational period (Figure 3 (c)), i.e., a water level setup at the landward side.

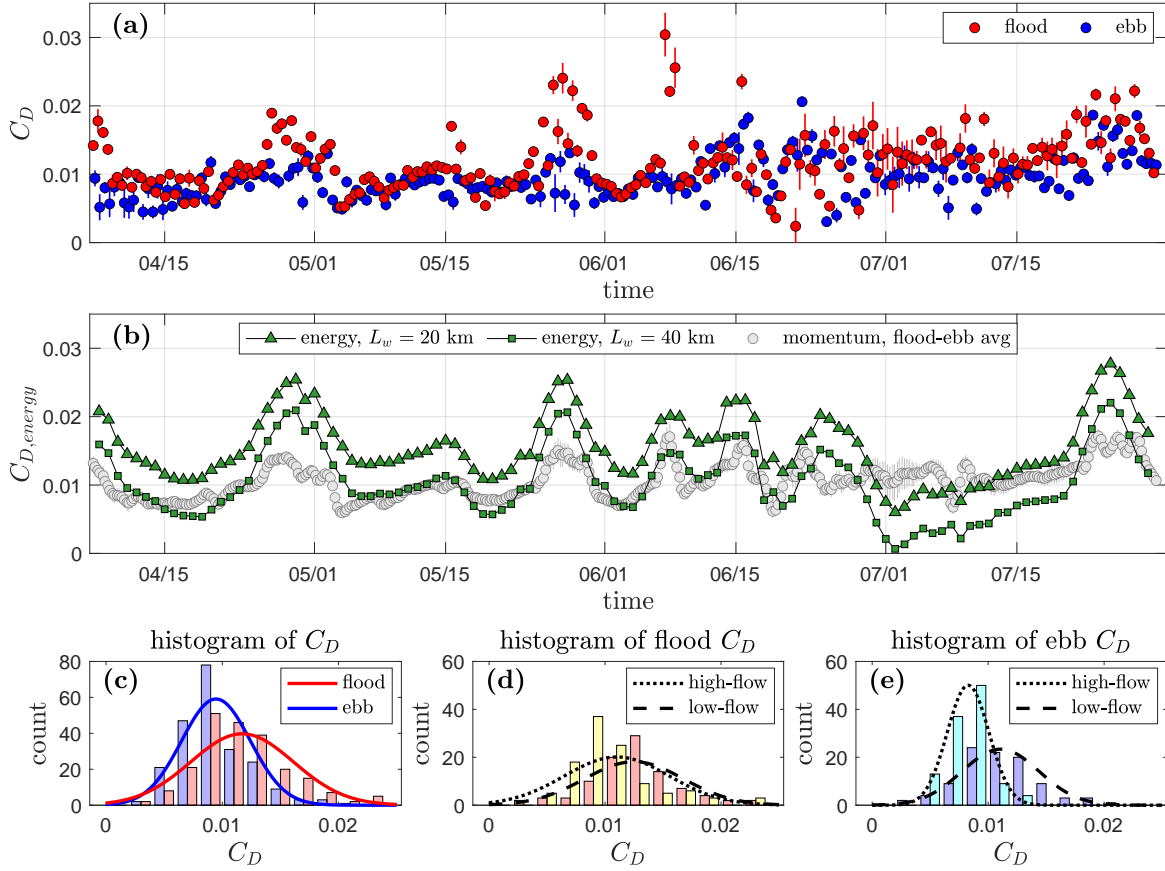


Figure 4: **(a)**: Drag coefficient  $C_D$  in the North River estuary calculated from the momentum balance. Red dots represent  $C_D$  at max flood tide; blue dots at max ebb tide. Vertical lines show the standard deviation within each 1-hr window around max flood and ebb tide. **(b)**: Drag coefficient  $C_{D,energy}$  calculated by energy flux balance. Yellow triangles are based on a width convergence distance  $L_w = 20$  km; orange triangles use  $L_w = 40$  km; gray circles are the flood-ebb averaged  $C_D$  from momentum balance in (a). **(c)**: Histograms of flood tide  $C_D$  and ebb tide  $C_D$ . **(d)**: Histograms of high-flow season flood  $C_D$  (before mid-June) and low-flow season flood  $C_D$  (after mid-June). **(e)**: Histograms of high-flow season ebb  $C_D$  and low-flow season ebb  $C_D$ . Lines show the Gaussian curve fits.

### 285 3.2 Drag

286 The drag coefficient  $C_D$  is calculated using (3) (Figure 4 **(a)**) and it represents the total momentum loss between  
 287 mooring sites LT1 and LT3. The total BTPG is the dominant term that balances the drag in the momentum budget,  
 288 similar to other studies in the coastal regions (e.g., Lentz et al., 2017; Rogers et al., 2018; Monismith et al., 2019).  
 289 The BCPG is about an order of magnitude smaller than the BTPG in most of the observational period, except during  
 290 neap tides and high discharge events when the BCPG can be up to 30% of the BTPG for ebb tides and 50% for flood  
 291 tides. The  $C_D$  values calculated from the mooring observations are generally in the range of  $5 \times 10^{-3} - 20 \times 10^{-3}$   
 292 (Figure 4 **(a)**).  $C_D$  values during both flood and ebb tides are higher than the typical values of  $\sim 3 \times 10^{-3}$  and  
 293 show large temporal variability. Averaging over the observation period,  $C_D$  is greater during flood tide ( $12 \times 10^{-3}$ )

294 than ebb tide ( $10 \times 10^{-3}$ ) (Figure 4 (c)). The highest calculated values (up to  $25 \times 10^{-3}$ ) correspond to flood tides,  
295 and flood tide  $C_D$  values are notably greater than ebb values during high spring tides, e.g., late April, late May and  
296 late July.

297 A seasonal difference can also be observed in ebb tide  $C_D$  (Figure 4 (e)). Most high values of  $C_D$  during ebb  
298 tide (e.g.,  $> 10 \times 10^{-3}$ ) are found in the low-flow season (starting from mid-June), resulting in a higher average  
299  $C_D$  in the low-flow season ( $11 \times 10^{-3}$ ) than in the high-flow season ( $8 \times 10^{-3}$ ). In contrast, flood tide  $C_D$  has a less  
300 clear seasonal difference (Figure 4 (d)), with average values of  $12.5 \times 10^{-3}$  in the low-flow season and  $11 \times 10^{-3}$   
301 during high flow.

302 It is worthwhile to note that the calculation of  $C_D$  includes the estimation of the time-mean BTPG (section 3.1).  
303 The seaward mean BTPG opposes the tidal BTPG during floods, and it is additive to the tidal BTPG during ebbs.  
304 The mean BTPG on average corresponds with an adjustment of  $C_D$  of  $2 - 3 \times 10^{-3}$  (20 - 30% of the total  $C_D$ ),  
305 and including the mean BTPG reduces the tidal asymmetry in the calculated  $C_D$ .

306  $C_{D,energy}$  is calculated from the energy flux balance using (13) (Figure 4 (b)) and it reflects the tidal energy  
307 dissipation. Generally  $C_{D,energy}$  is  $5 \times 10^{-3} - 20 \times 10^{-3}$  with the largest values during high spring tides, in  
308 agreement with the  $C_D$  from the momentum balance.  $C_{D,energy}$  calculated using  $L_w = 20$  km, as suggested by the  
309 exponential fitting (section 2), is generally greater than the tidally averaged  $C_D$  from the momentum budget. Using  
310  $L_w = 40$  km instead results in  $C_{D,energy}$  values that are more consistent with the momentum calculation.  $C_{D,energy}$   
311 has particularly low values around July 1 when the tidal amplitude increases from LT1 to LT3 (Figure 3 (a)). The  
312 overall high values of  $C_{D,energy}$  indicate a high rate of tidal energy dissipation that is broadly consistent with  
313 the high  $C_D$  calculated from the momentum balance. Moreover, the calculation of  $C_{D,energy}$  is independent of  
314 estimation of the mean BTPG since it is based on the tidal amplitude decay rate instead of the instantaneous water  
315 level gradient. The values of  $C_{D,energy}$  that are comparable with momentum-balance estimates of  $C_D$  provide  
316 corroborating evidence for the high values of effective drag coefficient.

317 In the following analysis, we used the  $C_D$  from the momentum balance, since it can be assessed for each flood  
318 and ebb tide and because it does not require estimation of the channel convergence rate.

### 319 **3.3 Local bottom shear stress**

320 The bottom friction coefficient  $C_f$  was estimated using both (14) and (16). The tidal-phase averaged values of  $C_f$   
321 from the ADV measurements are consistent between the two methods, and range between  $3 \times 10^{-3}$  and  $5 \times 10^{-3}$   
322 (Figure 5), which is similar to values for  $C_D$  due to bottom roughness in other estuaries (e.g., Heathershaw and  
323 Simpson, 1978; Seim et al., 2002). However,  $C_D$  calculated from the momentum balance during the same time

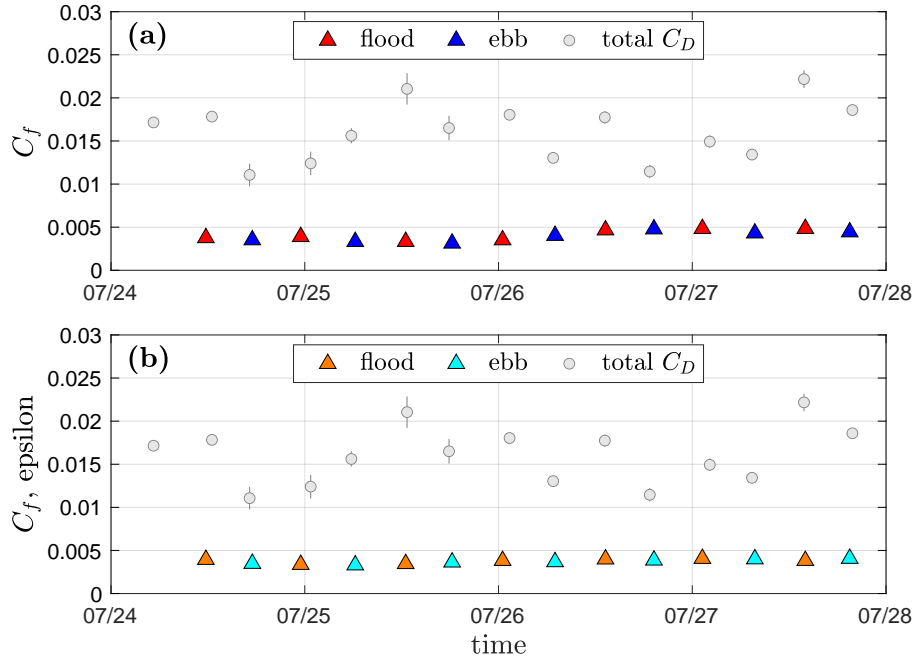


Figure 5: ADV measurement from July 24 to July 27. **(a)**: Bottom friction coefficient  $C_f$  calculated from the covariance method (14), (triangles, averaged over multiple ADV bursts in flood or ebb tides). Gray circles show the total  $C_D$  from momentum balance in Figure 4 (a) as a comparison. **(b)**: Bottom friction coefficient  $C_f$  calculated from the dissipation method (16).

324 period ranges between  $11 \times 10^{-3}$  and  $18 \times 10^{-3}$  for ebb tides and  $13 \times 10^{-3} - 22 \times 10^{-3}$  for flood tides. The total  
 325 drag  $C_D$  is larger than the bottom stress  $C_f$  by a factor of 3 – 5, indicating the existence of other sources of drag in  
 326 addition to bottom friction. Form drag due to flow separation at sharp channel bends could contribute to this high  
 327 total drag, as well as other potential factors including secondary circulation in bends, form drag from bedforms in  
 328 the channel, and friction from flow through marsh vegetation.

### 329 3.4 Dependence on water depth and discharge

330 Tides and river discharge provide the dominant forcing in this estuary, and we investigate the dependence of  $C_D$   
 331 on these two factors. Tidal conditions could affect the drag through creating variation in water level, velocity  
 332 amplitude, and flow structure. The calculated  $C_D$  does have a slightly increasing trend with water depth, with  
 333  $R^2 = 0.1$  and p-value  $< 0.001$  (Figure 6 (a)).  $C_D$  does not correlate with the tidal velocity ( $R^2 = 0.0$ , p-value  $>$   
 334  $0.05$ , not shown). The depth dependence primarily reflects the flood-ebb asymmetry in  $C_D$  noted previously. Water  
 335 levels are higher during flood tides than ebb tides (Figure 2 (a)), and flood tide  $C_D$  has a greater average value than  
 336 ebb tide  $C_D$ . The flood-ebb asymmetry in  $C_D$  is most apparent during high spring tides (Figure 4 (a)) when the  
 337 flood-ebb difference in water level is also greatest (Figure 2 (a)). In addition, zooming in on the cases with overbank

338 flow,  $C_D$  shows a decreasing trend with water depth for overbank flow conditions, opposite to the overall increasing  
 339 trend. Possible reasons for the observed depth dependence of  $C_D$  will be investigated in the following analysis.

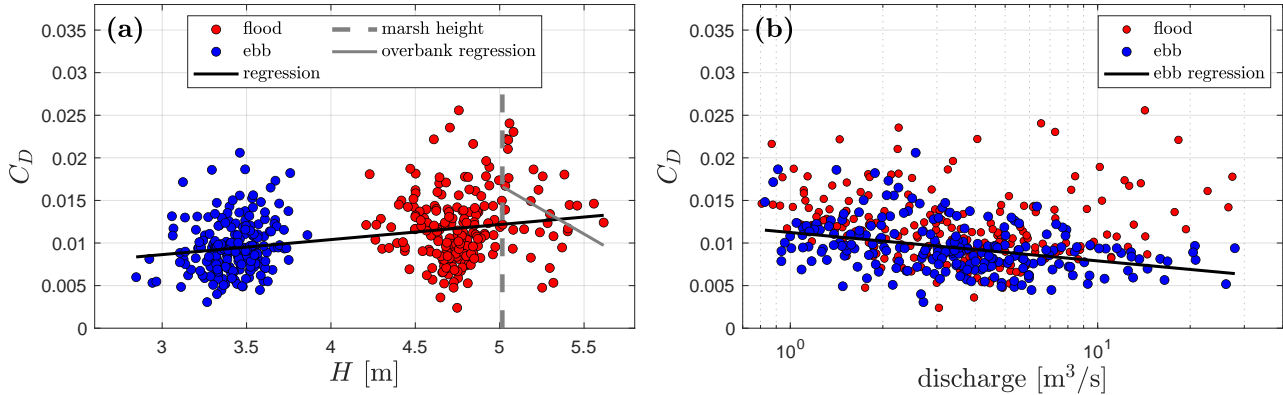


Figure 6: **(a)**: Drag coefficient vs. water depth at the bend apex. Linear regressions give  $R^2 = 0.10$  (p-value  $< 0.001$ ) for the overall data and  $R^2 = 0.14$  (p-value = 0.03) for the overbank cases (water depth exceeds marsh height). **(b)**: Drag coefficient vs. river discharge.  $R^2 = 0.13$  (p-value  $< 0.001$ ) for ebb tides, and  $R^2 = 0.00$  (p-value  $> 0.05$ ) for flood tides.

340 River discharge creates a seaward mean flow that influences the salt balance in addition to momentum, and  
 341 thus affects the salinity intrusion, along-estuary salinity gradient, and stratification (Geyer, 2010). The salinity field  
 342 affects the momentum budget through the along-estuary BCPG, and stratification can also reduce drag by damping  
 343 turbulence. In the observations, the ebb tide  $C_D$  has a negative correlation with river discharge (Figure 6 **(b)**). This  
 344 negative correlation is reflected in the seasonal trend in ebb tide  $C_D$ , where lower ebb  $C_D$  values occur during the  
 345 higher discharge season, and ebb  $C_D$  values increase in summer as river discharge decreases (Figure 4 **(e)**). In  
 346 contrast, the flood tide  $C_D$  shows no significant dependence on river discharge, and this corresponds with the less  
 347 apparent seasonal variation in flood  $C_D$  values (Figure 4 **(d)**). Factors that may be contributing to the observed  
 348 discharge dependence will also be addressed in the analysis.

## 349 4 Analysis

### 350 4.1 Flow separation and adverse pressure gradient

351 The high  $C_D$  in the North River estuary suggests the existence of other sources of drag beyond bottom friction,  
 352 and one source could be flow separation in the lee of bends (e.g., Leopold, 1960; Leeder and Bridges, 1975). An  
 353 idealized modeling study by Bo and Ralston (2020) found that flow separation in sinuous estuarine channels results  
 354 in significant form drag. In a sinuous channel with geometric parameters similar to the North River (e.g., bend  
 355 sharpness, aspect ratio), the total  $C_D$  increased to around  $12 \times 10^{-3}$  due to flow separation and the resulting form

356 drag. In the model results,  $C_D$  also increased with water depth in a manner consistent with the tidal differences in  
 357 water level and  $C_D$  observed in the North River (section 3.4). The positive depth-dependence in the model study  
 358 was because the flow separation and form drag became stronger in deeper water (Bo and Ralston, 2020).

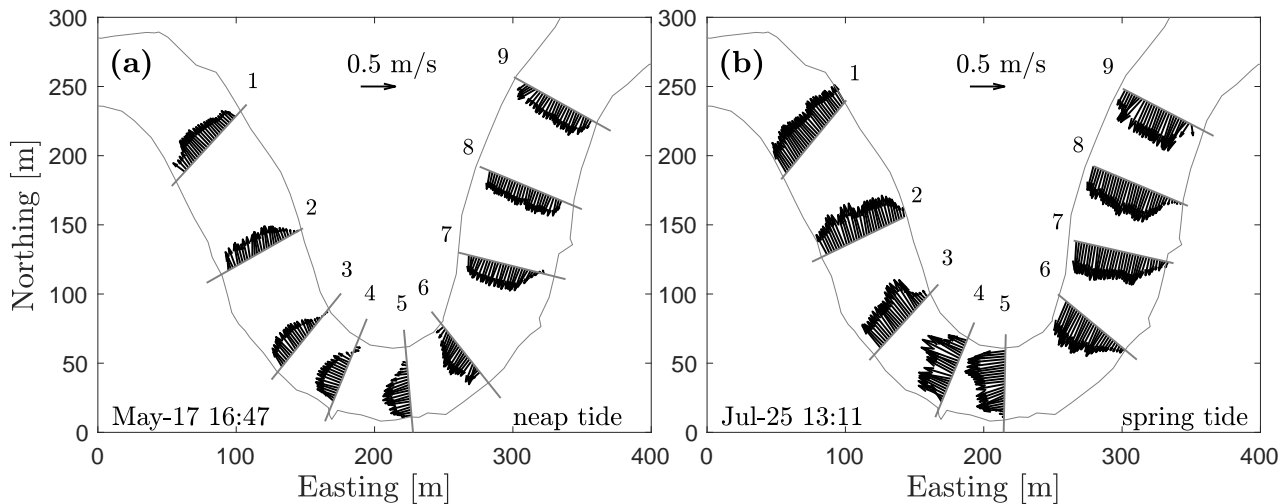


Figure 7: Depth-averaged velocity field during flood tides. (a): Neap flood tide in mid-May. (b): Spring flood tide in early July.

359 In the cross-channel ADCP surveys in the North River, flow separation was observed in the velocity field  
 360 downstream of the sharp bend (Figure 7). Depending on the tide, flow near the inner bank was decelerated relative  
 361 to the main current, and in some cases flow reversal was observed in the lee of the bend. Similar patterns of flow  
 362 separation and reversal were also found in field, laboratory, and modeling studies of curved channels, e.g., Ferguson  
 363 et al. (2003), Finotello et al. (2020), Blanckaert (2015), and Bo and Ralston (2020). In many river bends, point  
 364 bars form at the inner bank, and the shallower bathymetry there leads to topographic steering and contributes to the  
 365 deceleration of flow at the inner bank (e.g, Dietrich and Smith, 1983). In the North River bend, the cross-channel  
 366 bathymetry is relatively symmetric (section 2.1) so the deceleration and flow reversal near the inner bank is not  
 367 primarily due to topographic steering (Kranenburg et al., 2019). Instead the curvature effect on the pressure field is  
 368 likely the predominant mechanism for generating the observed flow separation.

369 The channel curvature results in a cross-channel water level slope at the apex of this bend (Kranenburg et al.,  
 370 2019), while the lateral differences in water level upstream and downstream of the bend are nearly zero. As a result,  
 371 the water level at the inner apex is lower than the downstream exit of the bend, and an adverse pressure gradient  
 372 occurs along the inner bank downstream of the apex. This adverse pressure gradient can lead to convex bank flow  
 373 separation and produce a low pressure “separation zone” in the lee of bends that thus creates the form drag (e.g.,  
 374 Ferguson et al., 2003; Blanckaert, 2010; Blanckaert et al., 2013; Bo and Ralston, 2020).

375 We examine the pressure gradient downstream of the bend apex to assess the potential for flow separation and  
 376 form drag. We have focused on the flood tide in the adverse pressure gradient analysis because the short-term (ST)  
 377 instrument array better resolved the local pressure gradient during the flood (section 2.2). The water level difference  
 378 ( $\Delta\eta$ ) between the CTD downstream of the bend (ST3A) and the CTD at the apex near the inner bank (ST2C) was  
 379 calculated to estimate the along-inner-bank pressure difference (Figure 8). In doing so, we have assumed that the  
 380 water level is laterally uniform at the downstream exit, and the ST3A measurement at the outer bank can represent  
 381 the inner bank water level. This assumption is reasonable because channel curvature is weak there (Figure 8 (d)),  
 382 and Kranenburg et al. (2019) reported negligible lateral water level differences at the exit of this bend. Note that  
 383 we have focused on the barotropic pressure, i.e., the water level, because the baroclinic pressure gradient is usually  
 384 much smaller.

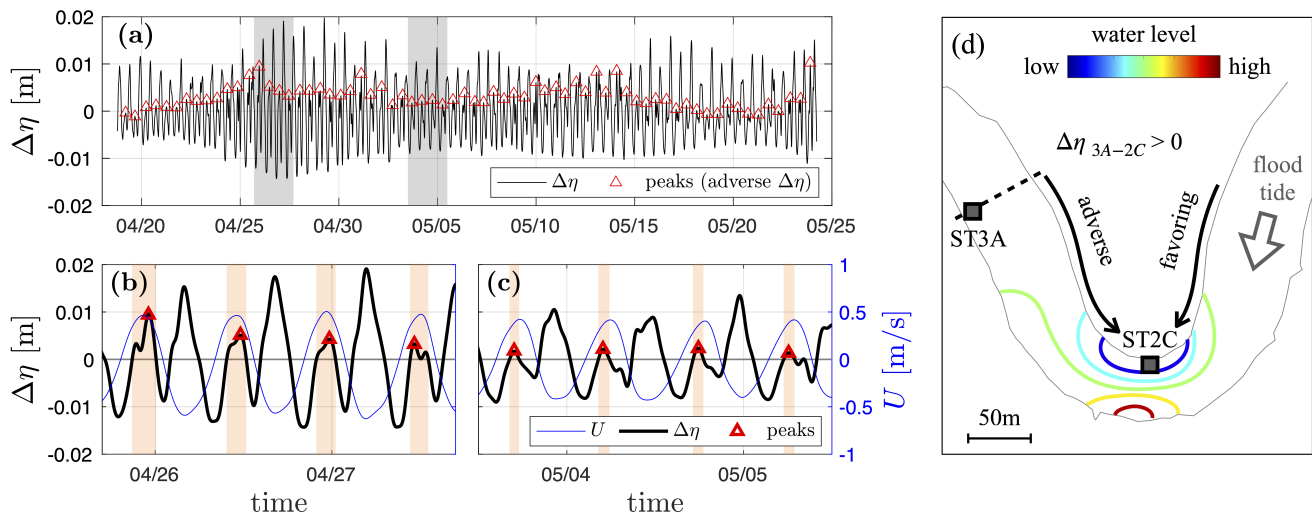


Figure 8: **(a)**: Water level difference ( $\Delta\eta$ ) between CTDs ST3A and ST2C. Red triangles mark the peaks of adverse  $\eta_s$ . The gray bands represent the zoomed-in time periods shown in panels **(b)** and **(c)**. **(b)**, **(c)**:  $\Delta\eta$  and adverse  $\Delta\eta$  in late April (spring tide) and early May (neap tide). The left vertical axis shows  $\Delta\eta$  (black line) and the right vertical axis shows  $U$  (blue line) – the depth-averaged velocity at the apex. Orange bands mark the periods when adverse pressure gradient appears.  $U > 0$  is flood tide. **(d)**: A schematic of the adverse pressure gradient in the bend, with contours of the water level field.

385 The water level difference  $\Delta\eta$  is positive during ebb tide (Figure 8), consistent with the downstream favoring  
 386 pressure gradient that drives the seaward current. Entering flood tide, the flow direction turns and  $\Delta\eta$  becomes  
 387 negative, consistent with a favoring pressure gradient. However, as the landward tidal current keeps growing, the  
 388 adverse pressure gradient associated with the curvature effect occurs and this can be seen in the upward peaks in  
 389  $\Delta\eta$  during flood tides in Figure 8. This positive, or adverse,  $\Delta\eta$  around max flood tide creates the adverse pressure  
 390 gradient downstream of the bend along the inner bank that corresponds with flow separation.

391 To assess the potential influence of flow separation and form drag on the observed  $C_D$ , we examine the cor-

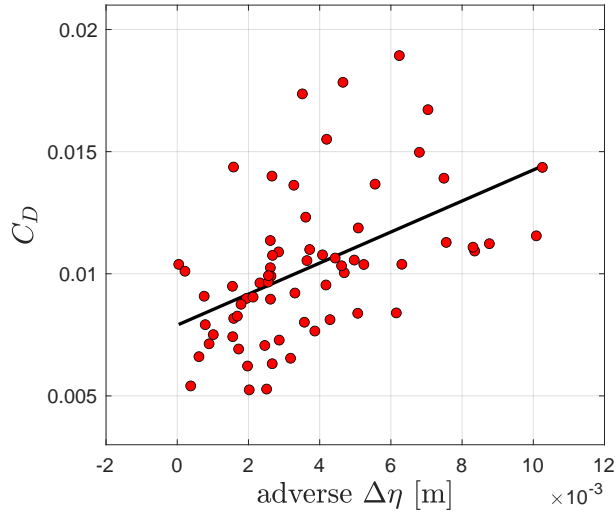


Figure 9: Correlation between the drag coefficient and adverse  $\Delta\eta$  that appears at flood tide.  $R^2 = 0.25$  (p-value  $< 0.001$ ).

392 relation between the drag and adverse pressure gradient along the inner bank. The adverse pressure gradient was  
 393 calculated using the short-term measurements (in April and May), so only the corresponding part of the  $C_D$  record  
 394 (calculated using the long-term moorings) is examined. The  $C_D$  calculated from the large-scale LT measurements is  
 395 significantly correlated with the bend-scale adverse  $\Delta\eta$  from ST measurements ( $R^2 = 0.25$  and p-value  $< 0.001$ ),  
 396 with  $C_D$  increasing as the adverse pressure gradient increases (Figure 9). While the spatial and temporal coverage  
 397 of the observational data is limited, the trends in the available evidence are consistent with the explanation that flow  
 398 separation, as reflected in the strength of the adverse pressure gradient measured at the sharp bend of the study,  
 399 contributes to the high drag found in the North River estuary.

400 The adverse pressure gradient for ebb tide is not investigated due to the lack of pressure measurement at the  
 401 down-estuary exit of the bend. Flow separation was also observed in the ebb tide velocity field with decelerated  
 402 flow near the inner bank (not shown), although the velocity field during ebb is also affected by topographic steering  
 403 associated with the relatively shallow shoal near the inner bank at the down-estuary side of the bend (Figure 1).  
 404 According to the previous idealized modeling results, flow separation is expected to be weaker during ebb tide  
 405 because of the shallower water depth and greater influence of friction (Bo and Ralston, 2020).

## 406 4.2 Overbank flow

407 During high spring tides, the water level exceeds channel bank height and marshes are inundated. The marsh height  
 408 at the bend apex corresponds to a water depth of  $\sim 5$  m. The high spring tides in late May and late July are plotted  
 409 in Figure 10 as an example. Water level displays a diurnal variation due to the K1 tidal component and channel

410 flow substantially goes onto the marsh at the higher flood tide, every other tidal cycle.

411 The drag coefficient also shows a diurnal variation, with  $C_D$  that is smaller during the flood tides that have  
 412 overbank flow compared to the prior and subsequent tides. The marsh platform is vegetated, and the overbank flow  
 413 through the marsh vegetation might be expected to increase the total drag due to stem friction. Instead, the total  
 414 drag is decreased with overbank flow. The reduced values of  $C_D$  during flood tides with overbank flow also is  
 415 counter to the overall relationship of drag increasing with water depth (Figure 6 (a)), and is opposite to the depth  
 416 dependence expected from flow separation (Bo and Ralston, 2020).

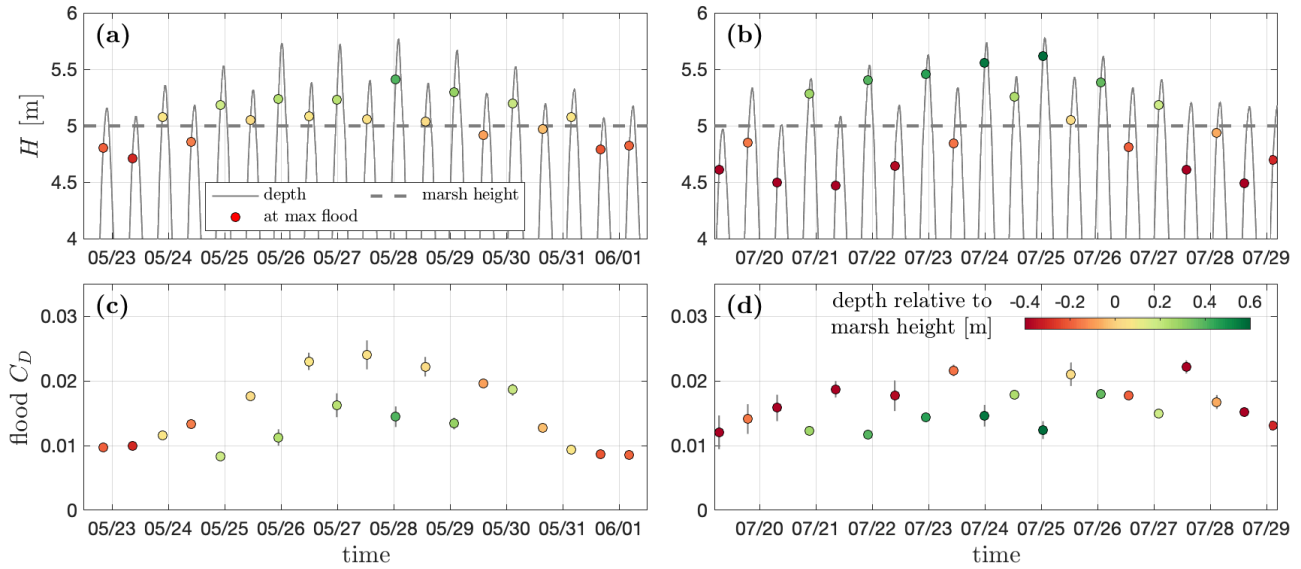


Figure 10: Water depth  $H$  and flood-tide drag coefficient  $C_D$  during high spring tides in late May and late July. (a): Water depth in late May; (b): water depth in late July; (c): flood tide  $C_D$  in late May; (d): flood tide  $C_D$  in late July.

417 A potential explanation for the decrease in  $C_D$  with overbank flow could relate to the inhibition of flow separa-  
 418 tion. While deeper water facilitates flow separation, increased bottom friction due to the shallow overbank flow  
 419 and stem friction from flow through vegetation could inhibit flow separation. The frictional effect is illustrated by  
 420 dimensionless numbers from theoretical models that predict flow separation, e.g.,  $H/(C_f W)$  in Blanckaert (2010)  
 421 where  $H$  is water depth,  $C_f$  is the friction coefficient, and  $W$  is channel width, and  $H/(C_f L)$  in Bo and Ralston  
 422 (2020) with  $L$  being the bend length. The underlying mechanism of these theoretical models is that stronger bottom  
 423 friction diminishes the local adverse pressure gradient along the inner bank and inhibits flow separation. The effective  
 424  $C_f$  increases for overbank flow because of both the shallower water depth over the marsh and the stem friction  
 425 of vegetation. As a result, flow separation that creates form drag is inhibited when flow goes onto the marsh and  
 426 the total drag is decreased, even though locally flow over the marsh has relatively large friction. The overbank flow  
 427 effect is reflected in the depth dependence plot, where  $C_D$  shows a decreasing trend when water depth exceeds the

428 marsh platform height (Figure 6 (a)). Similar results were reported for laboratory experiments by Marriott (1998)  
 429 where flow separation occurred in a sinuous channel but did not occur when flow was overbank. Similarly, James  
 430 et al. (2001) found that vegetation can inhibit flow separation in sinuous laboratory channels and decrease the total  
 431 drag, consistent with the decreased  $C_D$  for flow over the marsh in the North River estuary.

### 432 4.3 Stratification and baroclinic effects

433 The dependence of  $C_D$  on river discharge (Figure 6 (b)) suggests that baroclinic effects may play a role in flow  
 434 separation and the drag. In this subsection, we describe an observed interaction between stratification and secondary  
 435 circulation during ebb tides, and propose a baroclinic mechanism that can potentially reduce the adverse pressure  
 436 gradient along the inner bank, and thereby inhibit flow separation and decrease the drag.

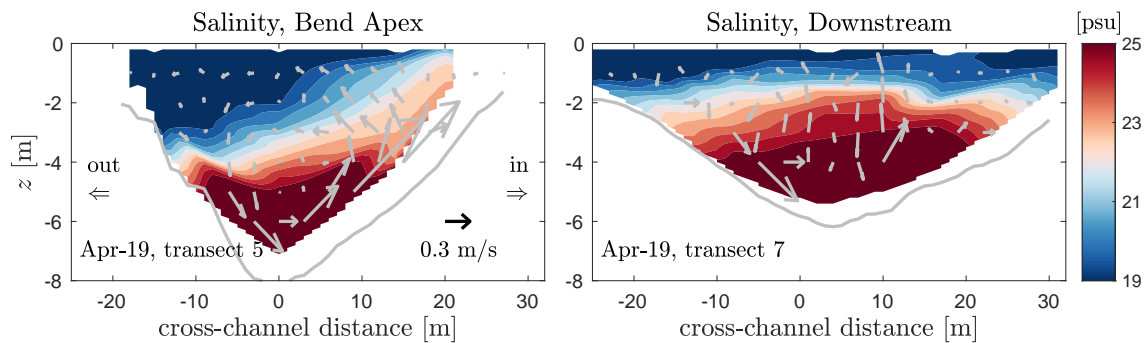


Figure 11: Salinity and secondary circulation in two cross-sections at the apex (transect 5) and downstream (transect 7) during an early ebb tide with strong stratification.

437 During ebb tides, a normal secondary circulation is observed in the cross-section at the apex (Figure 11). When  
 438 the channel is stratified, this normal secondary circulation brings high salinity water to the inner bank and tilts the  
 439 isohalines up near the bend apex. Downstream of the bend, the lateral circulation is weaker and has less effect on  
 440 the lateral salinity distribution, so the isohalines are relatively flat. Similar isohaline tilting has been observed in,  
 441 e.g., Seim and Gregg (1997); Chant (2002). The lateral circulation resulting from flow curvature creates a bulge of  
 442 high salinity water near the inner bank at the bend apex. During the ebb, this high salinity at the inner bank of the  
 443 apex exerts a favoring baroclinic pressure gradient downstream of the apex that counteracts the adverse barotropic  
 444 pressure gradient downstream of the bend created by the flow curvature (section 4.1). Consequently, the interaction  
 445 between the lateral circulation and stratification could inhibit flow separation, and reduce the form drag around  
 446 bends.

447 The next question is whether the favoring baroclinic pressure gradient along the inner bank due to the lateral  
 448 circulation is large enough to balance the barotropic adverse pressure gradient created by the curved streamwise

449 flow. The baroclinic pressure gradient can be directly calculated using  $\beta g(\partial S_{in}/\partial s)H_{in}$ , where  $S_{in}$  and  $H_{in}$  are  
 450 the depth-averaged salinity and depth at the inner bank. The barotropic pressure gradient is estimated from the  
 451 along-inner-bank momentum balance

$$g \frac{\partial \eta_{in}}{\partial s} = -U_{in} \frac{\partial U_{in}}{\partial s} - C_f \frac{U_{in}|U_{in}|}{H_{in}} = adv. + frict., \quad (18)$$

452 where  $U_{in}$  is the depth-averaged velocity at the inner bank. On the right side of (18) are the advection and friction  
 453 terms that determine adverse pressure gradient and flow separation in homogeneous fluids (Bo and Ralston, 2020).  
 454 The barotropic and baroclinic pressure gradients are estimated using the cross-channel surveys during an early  
 455 ebb tide on April 19 (transects 5 and 7, Figure 7).  $U_{in}$  and  $H_{in}$  are calculated from the cross-channel ADCP  
 456 measurements and  $S_{in}$  is from the shipboard CTD measurements, each taken as the average over 10 m from the  
 457 inner bank ( $S_{in} = 22.6$  psu at transect 5 and  $S_{in} = 20.9$  psu at transect 7, Figure 11). The advection term  
 458 contributes to an adverse pressure gradient and the friction term contributes to a favoring pressure gradient, which  
 459 is consistent with theoretical models that predict flow separation in Signell and Geyer (1991) and Bo and Ralston  
 460 (2020). The barotropic pressure gradient that is the sum of the advection and friction terms is positive ( $\sim 1$  to  
 461  $6 \times 10^{-4}$  m/s<sup>2</sup>), indicating an adverse pressure gradient that can cause flow separation downstream of the apex. In  
 462 contrast, the baroclinic pressure gradient is negative ( $\sim -2 \times 10^{-4}$  m/s<sup>2</sup>) and can counteract the adverse pressure  
 463 gradient. Downstream of the apex, the favoring baroclinic pressure gradient is of the same order of magnitude as the  
 464 adverse barotropic pressure gradient, suggesting that the salinity effect has the potential to inhibit flow separation.

465 This baroclinic inhibition of flow separation may explain the variation in ebb tide  $C_D$  with the river discharge  
 466 (Figure 6 (b)). The along-inner-bank baroclinic pressure gradient results from the interaction between the stratifi-  
 467 cation and secondary circulation during the ebb tide. Stratification is stronger in the high-flow season, which can  
 468 lead to stronger baroclinic pressure gradients and weaker flow separation, and thus reduce ebb tide  $C_D$ . Under  
 469 low-flow conditions, stratification is weak, and while the lateral circulation is still present, the baroclinic pressure  
 470 gradient due to tilting of isopycnals disappears.

471 The direct effects of stratification on damping turbulence and reducing the bottom friction could be another  
 472 reason for the observed negative correlation between ebb tide  $C_D$  and discharge. Stratification becomes stronger  
 473 during higher discharge periods and it can inhibit turbulence (Geyer, 1993), alter vertical momentum distribution,  
 474 and decrease the bottom shear stress. However, the bottom stress is not the dominant contributor to the total  $C_D$   
 475 (section 3.3), and the inhibition of bottom friction alone is insufficient to explain the discharge dependence of  $C_D$ .  
 476 The variation in ebb tide  $C_D$  with river discharge is more than  $5 \times 10^{-3}$  (Figure 6 (b)), which is greater than the

477 local estimates of  $C_f$  (Figure 5).

478 The ebb tide  $C_D$  is negatively correlated with  $\Delta S$ , but the correlation only holds for  $\Delta S$  during the early ebb  
479 ( $R^2 = 0.2$  and p-value  $< 0.001$ ) not for  $\Delta S$  at max ebb tide ( $R^2 = 0.0$  and p-value  $> 0.05$ ) because stratification  
480 has typically mixed away by max ebb.  $C_D$  is calculated from the momentum balance around max ebb tide (sec-  
481 tion 2.3.1), suggesting that the inhibition of flow separation by stratification has a lagged effect. Stratification can  
482 impede the growth of adverse pressure gradient during early ebb tide so that flow separation is not fully developed  
483 at max ebb, even if stratification has disappeared at that time. In contrast, the inhibition of bottom shear stress by  
484 stratification happens instantaneously. Any inhibition of turbulence and bottom shear stress by stratification during  
485 early ebb is unlikely to affect bottom shear stress at max ebb, which further indicates that the discharge dependence  
486 of  $C_D$  is not due to the direct inhibition of turbulence by stratification.

487 The secondary circulation is more complex during flood tide, as the sense of secondary circulation can be  
488 reversed and multiple circulation cells are formed (Kranenburg et al., 2019). The interaction between stratification  
489 and the secondary circulation during flood tide, as well as any influence on flow separation and drag are still  
490 unknown.

#### 491 **4.4 Bed roughness**

492 The bottom friction appears to contribute less than form drag to the increased total drag, given that the bottom  
493 friction coefficient  $C_f$  is around  $3 \times 10^{-3} - 5 \times 10^{-3}$ , much smaller than the total drag coefficient  $C_D$  (sections 3.2  
494 and 3.3). The  $C_f$  calculation was based on the ADV measurements near the apex of bend, and the calculated  $C_f$   
495 values correspond with a log-layer estimate for the bottom roughness of  $z_0 = 0.002 - 0.005$  m (e.g., Lentz et al.,  
496 2017). However, the bathymetry survey of the North River (section 2.2) indicates that the bedforms vary in size  
497 along the estuary, and that in some areas the bed roughness elements may be much larger than this local estimate  
498 from the ADV would suggest.

499 We estimate the bottom roughness scales quantitatively by using the detrended bathymetry data following an  
500 approach as in Rogers et al. (2018). Mega ripples are found at several locations near the sharp bend with roughness  
501 height  $h_b$  of 0.1 – 0.5 m and wavelength  $\lambda_b$  of 1 – 10 m, and bedform crests are generally oriented perpendicular to  
502 the along-channel flow. The bedform steepness  $h_b/\lambda_b$  is generally in the range of 0.05 – 0.1. The bottom roughness  
503  $z_0$  due to these bedforms is estimated as

$$z_0 = a_1 h_b \frac{h_b}{\lambda_b}, \quad (19)$$

504 where  $a_1$  is a linear roughness coefficient (e.g., Grant and Madsen, 1982; Rogers et al., 2018).  $a_1$  is typically in

505 the range of 0.3 – 3 (Soulsby, 1997; Trowbridge and Lentz, 2018) and here we assume  $a_1 = 1$  as an estimate.  
506 Based on this, the mega ripples in the North River correspond to a  $z_0$  of 0.002 – 0.05 m and a depth-averaged drag  
507 coefficient of up to 0.01 (Lentz et al., 2017). These higher values of  $z_0$  apply only in parts of the estuary rather  
508 than everywhere, so bottom roughness alone does not explain the observed high drag. In addition, the  $C_f$  due to  
509 bottom roughness typically has a decreasing trend with increasing water depth (Lentz et al., 2017), opposite to the  
510 observed depth dependence, so bottom roughness does not explain the variability of the total  $C_D$  with water depth.  
511 However, these large scale bottom features could be an important factor locally, and the combined effects of the  
512 multiple scales of bottom roughness on the overall drag still requires further investigation.

## 513 **5 Discussion**

### 514 **5.1 Explaining the high drag and its large variability**

515 We observed that the effective drag coefficients were greater than expected from bottom friction alone in the North  
516 River estuary. Multiple lines of evidence suggest that form drag due to flow separation at channel bends is a leading  
517 factor in the high drag observed in the North River. The high values of  $C_D$  are consistent with modeling results  
518 in sinuous channels with similar geometric parameters in Bo and Ralston (2020) where  $C_D$  was dominated by  
519 form drag due to flow separation. The correlation between the observed adverse pressure gradients and  $C_D$  is  
520 also consistent with the explanation that the high  $C_D$  is associated with flow separation and form drag. The high  
521  $C_D$  shows a flood-ebb asymmetry that is most apparent during high spring tides, which corresponds with a depth  
522 dependence of  $C_D$  due to higher water levels around max flood. This positive correlation with depth is consistent  
523 with the response expected for form drag due to flow separation based on idealized and theoretical models. This  
524 suggests that  $C_D$  values are higher during flood tides than ebb tides because the deeper water during flood tides  
525 leads to stronger flow separation and greater form drag.

526 Diurnal variations in flood tide  $C_D$  appear to correspond with the diurnal inundation of the marsh platform  
527 during spring tides, and  $C_D$  is decreased when the marsh is inundated. As a result,  $C_D$  has the opposite trend with  
528 water depth when flow is above the channel banks compared with the rest of the data. A potential explanation for  
529 this trend is that the local increase in friction with overbank flow inhibits flow separation and reduces the form drag.

530 The ebb tide  $C_D$  has a decreasing trend with river discharge, while the flood tide  $C_D$  does not depend on  
531 discharge. Stratification increases with river discharge, and the correlation between discharge and ebb  $C_D$  may  
532 be due to interaction between the stratification and lateral circulation that results in a local baroclinic pressure  
533 gradient that inhibits flow separation. While direct field evidence is lacking, the observations are suggestive that

534 baroclinicity can influence flow separation in estuarine channels. The direct influence of stratification on damping  
535 turbulence and reducing drag appears to be less important here, due to the relatively weak stratification during  
536 periods with the strongest tidal velocities.

537 We have focused on the role of flow separation and form drag in the momentum budget and the high  $C_D$ , but  
538 the role of form drag in the tidal energy flux in the North River estuary is still unclear.  $C_{D,energy}$  generally has  
539 similar magnitudes to  $C_D$ , suggesting that the high energy dissipation is consistent with the high drag. However,  
540 the  $C_{D,energy}$  calculated based on the channel convergence rate, i.e.,  $L_w = 20$  km, is higher than  $C_D$  during  
541 most of the observational period (Figure 4 (b)). While uncertainty in the channel geometry estimation could be an  
542 explanation, the discrepancy may also relate to differences in how form drag and bottom friction lead to energy  
543 loss. Typically the dissipation caused by bottom friction is scaled with the bottom stress times tidal velocity  $\|U\|$   
544 (e.g., van Rijn, 2011), but the appropriate velocity for scaling the dissipation associated with form drag is more  
545 uncertain (MacCready et al., 2003). The fact that  $C_{D,energy}$  (based on  $L_w = 20$  km) is higher than  $C_D$  from the  
546 momentum budget suggests that the effect of form drag in leading to energy dissipation may be overestimated by  
547 (13), i.e., the dissipation due to form drag needs to be scaled with a smaller velocity than  $\|U\|$ .

## 548 **5.2 Other factors contributing to the high drag**

549 While flow separation and form drag appear to play an important role in the high drag observed in the North River,  
550 other process may also contribute. Secondary circulation due to curvature and baroclinic forcing is strong in the  
551 North River (Kranenburg et al., 2019). Interactions between the secondary circulation and lateral salinity distri-  
552 bution may influence the form drag from flow separation (section 4.3), but secondary circulation can also directly  
553 increase the drag by creating stronger near-bed lateral velocity and by redistributing the streamwise momentum  
554 (e.g., Blanckaert and de Vriend, 2003). The near-bottom streamwise velocity ranges between 0.2 and 0.6 m/s at  
555 max flood and ebb and the near-bottom lateral velocity is 0 – 0.3 m/s. The ratio of bottom lateral velocity to  
556 streamwise velocity is 0.4 – 0.5 on average, so based on the quadratic dependence of drag we can estimate that  
557 the lateral velocity may increase the bottom shear stress by 20 – 30%. The effects of the redistribution of stream-  
558 wise momentum by the lateral circulation are harder to estimate. The downward vertical velocity associated with  
559 secondary circulation advects greater streamwise velocity toward the bed and squeezes the boundary layer, and the  
560 increased velocity variance and thinner boundary layer enhance the local bottom friction. Consequently, secondary  
561 circulation can change the bottom stress distribution in channel bends and increase the overall drag.

562 In addition to flow separation and secondary circulation in channel bends, smaller-scale roughness elements can  
563 also influence the drag. The bed roughness features of the mid-estuary region have been analyzed in section 4.4,

564 but the integrated effects of multiple scales of bedforms and features like point bars and shallow shoals that can  
565 affect the drag still need to be studied. The sharp studied bend does not have a distinct point bar at the apex and  
566 nor do other bends in the mid-estuary region. Shallow bathymetry near the inner bank can enhance local friction  
567 and inhibit flow separation, so the absence of a point bar increases the tendency for flow separation in the North  
568 River estuary. Kranenburg et al. (2019) suggested that the reversed secondary circulation in this bend, with outward  
569 current near the bed, can limit sediment deposition at the inner bank and inhibit development of a point bar. Flow  
570 separation may be another reason for the relatively symmetric cross-channel bathymetric profile at the bend apex.  
571 A separation zone near the inner bank restricts the effective channel width at the apex and accelerates flow in  
572 the middle channel, and the accelerated velocity can maintain the deep scour at the center of the channel (e.g.,  
573 Vermeulen et al., 2015). Despite lack of point bars, several shoals were found in the bends (e.g., Figure 1). These  
574 shallow bathymetry features create intermediate-scale roughness in bend flows (larger than bedforms but smaller  
575 than bend-scale) and may influence the total drag by affecting the bottom stress, the secondary circulation patterns,  
576 or the form drag of flow separation in bends.

## 577 **6 Conclusion**

578 We observe in an estuary with channel curvature that the drag coefficients are  $5 \times 10^{-3} - 20 \times 10^{-3}$ , much greater  
579 than expected from bottom friction alone.  $C_D$  varies at both tidal and seasonal time scales. The  $C_D$  values are  
580 greater during flood tides than ebb tides, particularly during high spring tides. The tidal asymmetry corresponds  
581 with a  $C_D$  that increases with water depth. Ebb tide  $C_D$  decreases with river discharge but flood tide  $C_D$  shows no  
582 dependence on discharge. We observe flow reversal and adverse pressure gradients at the inside of a sharp bend,  
583 and the analysis shows that flow separation and the associated form drag is a leading factor in the high total drag.  
584 During the highest spring tides, decreased values of  $C_D$  were found for overbank flow cases, and that is explained  
585 by an inhibition of flow separation due to the locally increased friction. Similarly, baroclinic effects during ebbs  
586 may inhibit flow separation and explain the decreasing trend with discharge. Other factors may also contribute to  
587 the drag including secondary circulation, multiple-scales of bedforms, and shallow shoals, but the various lines of  
588 evidence suggest that flow separation plays a key role in the high total drag.

## 589 **A Mean along-estuary momentum balance**

590 The depth-integrated along-channel momentum equation is (Nihoul and Ronday, 1975)

$$\frac{\partial q}{\partial t} + \frac{\partial}{\partial s} \left( \frac{q^2}{h} \right) = -gh \frac{\partial \eta}{\partial s} - \frac{C_f}{h^2} q |q| - \frac{\partial}{\partial s} \int_{-h_0}^{\eta} \int_z^{\eta} \beta g S dz dz, \quad (20)$$

591 where we have neglected wind stress and assumed no bottom slope.  $q$  is the depth-integrated flux.  $h$  is the total  
 592 water depth,  $\eta$  is water level, and  $h_0$  is the bathymetry depth.  $h = h_0 + \eta$ .  $S$  is salinity.  $C_f$  is the bottom friction  
 593 coefficient.  $q$  is given as

$$q = \int_{\eta-h}^{\eta} u dz = Uh, \quad (21)$$

594 with  $u$  being the streamwise velocity and  $U$  being the depth average.  $\eta$  is

$$\eta = \bar{\eta} + \eta', \quad (22)$$

where  $\eta'$  is the measured water level fluctuations and  $\bar{\eta}$  is the mean water level that was not directly resolved in  
 the North River observations. We use an overbar to denote time averages of other properties and a prime to denote  
 temporal fluctuations, so

$$q = \bar{q} + q', \quad (23a)$$

$$U = \bar{U} + U', \quad (23b)$$

$$h = \bar{h} + \eta', \quad (23c)$$

$$\bar{h} = h_0 + \bar{\eta} \sim h_0. \quad (23d)$$

595 The mean along-estuary momentum balance can be derived by taking the time average of (20), where the  
 596 unsteady term is zero after averaging and the other three nonlinear terms in (20) can lead to time-mean forcing.  
 597 Averaging the water level gradient term in (20) gives rise to two terms,

$$\overline{gh \frac{\partial \eta}{\partial s}} = g \bar{h} \frac{\partial \bar{\eta}}{\partial s} + g \overline{\eta' \frac{\partial \eta'}{\partial s}}. \quad (24)$$

598 The first term on the right side is the mean barotropic pressure gradient (BTPG, or water level gradient forcing)

599 and the second term relates to the tidal stress  $\tau_t$ .

$$\tau_t = -\rho g \eta' \frac{\partial \eta'}{\partial s}. \quad (25)$$

600 The tidal stress, as a manifestation of the radiation stress from a tidal wave (Zimmerman, 1978), has been reported  
 601 in observational studies including on the North Sea (Prandle, 1978) and in San Francisco Bay (Walters and Gartner,  
 602 1985). Rearranging (25) and assuming sinusoidal tides,

$$\tau_t = -\frac{1}{2} \rho g \frac{\partial(\eta'^2)}{\partial s} = -\frac{1}{4} \rho g \frac{\partial}{\partial s} (\|\eta\|^2), \quad (26)$$

603 where  $\|\eta\|$  is the norm of tidal water level fluctuation, i.e., tidal amplitude.

604 Averaging the advection term in (20), we get

$$\frac{\partial}{\partial s} \left( \frac{q^2}{h} \right) \sim \frac{1}{h} \frac{\partial}{\partial s} (q^2). \quad (27)$$

605 The mean forcing associated with the advection term is generally small. Moreover, velocity is nonuniform laterally  
 606 due to bathymetry variation and channel curvature, so the along-channel flux gradient based on measurements at a  
 607 single location in the North River estuary is not representative for use in this estimate. Therefore, we have neglected  
 608 this advection term in the mean momentum balance.

609 The average of the frictional term in (20) represents the friction of the mean flow, which consists of the freshwa-  
 610 ter discharge and the Eulerian return flow of the landward Stokes drift of the tidal wave (Zimmerman, 1979; Uncles  
 611 and Jordan, 1980). For estuaries with small or moderate discharge (e.g., the North River estuary),  $\bar{U} \ll \|U\|$ , where  
 612  $\|U\|$  is the norm of tidal velocity  $U'$ . The mean flow friction  $\tau_{b,\bar{u}}$  can thus be estimated as (e.g., Parker, 2007)

$$\tau_{b,\bar{u}} = -\frac{\overline{C_f}}{h^2} \rho q |q| = -\overline{C_f \rho U |U|} = -\frac{4}{\pi} C_f \rho \|U\| \bar{U}. \quad (28)$$

613 Averaging the salinity gradient term in (20) yields the mean baroclinic pressure gradient (BCPG) forcing

$$-\frac{\partial}{\partial s} \int_{-h_0}^{\eta} \int_z^{\eta} \beta g S dz dz \approx -\frac{1}{2} \beta g h^2 \frac{\partial \langle S \rangle}{\partial s} \approx -\frac{1}{2} \beta g h \frac{\partial \langle S \rangle}{\partial s} \bar{h}, \quad (29)$$

614 where  $\langle S \rangle$  is the depth-averaged salinity.

615 Therefore, in the mean momentum budget, the mean BTPG is balanced with three terms, the tidal stress  $\tau_t$ , the

616 mean flow friction  $\tau_{b,\bar{u}}$ , and the mean BCPG. The mean BTPG can be estimated as

$$g \frac{\partial \bar{\eta}}{\partial s} = \frac{1}{\rho h} (\tau_t + \tau_{b,\bar{u}}) - \overline{\frac{1}{2} \beta g h \frac{\partial \langle S \rangle}{\partial s}}, \quad (30)$$

617 where  $\tau_t$  and  $\tau_{b,\bar{u}}$  are given by (26) and (28). We have compared the estimation from (30) with the mean BTPG in  
 618 model results from Bo and Ralston (2020), and found that the estimation agrees well ( $R^2 = 0.85$ ).

619 We calculated  $\tau_t$ ,  $\tau_{b,\bar{u}}$ , and the mean BCPG from the observations in the North River estuary (section 2.3.2)  
 620 and examined their dependence on tides and discharge (Figure A.1).  $\tau_t$  is primarily dependent on tides, and as  
 621 the tidal amplitude increases, the tidal decay rate increases and the tidal stress becomes stronger. Freshwater  
 622 discharge creates the mean river flow and tides can lead to a return flow, and therefore,  $\tau_{b,\bar{u}}$  is correlated with both  
 623 discharge and tidal amplitude. The mean BCPG has a negative correlation with tidal amplitude and a weak positive  
 624 dependence on discharge.

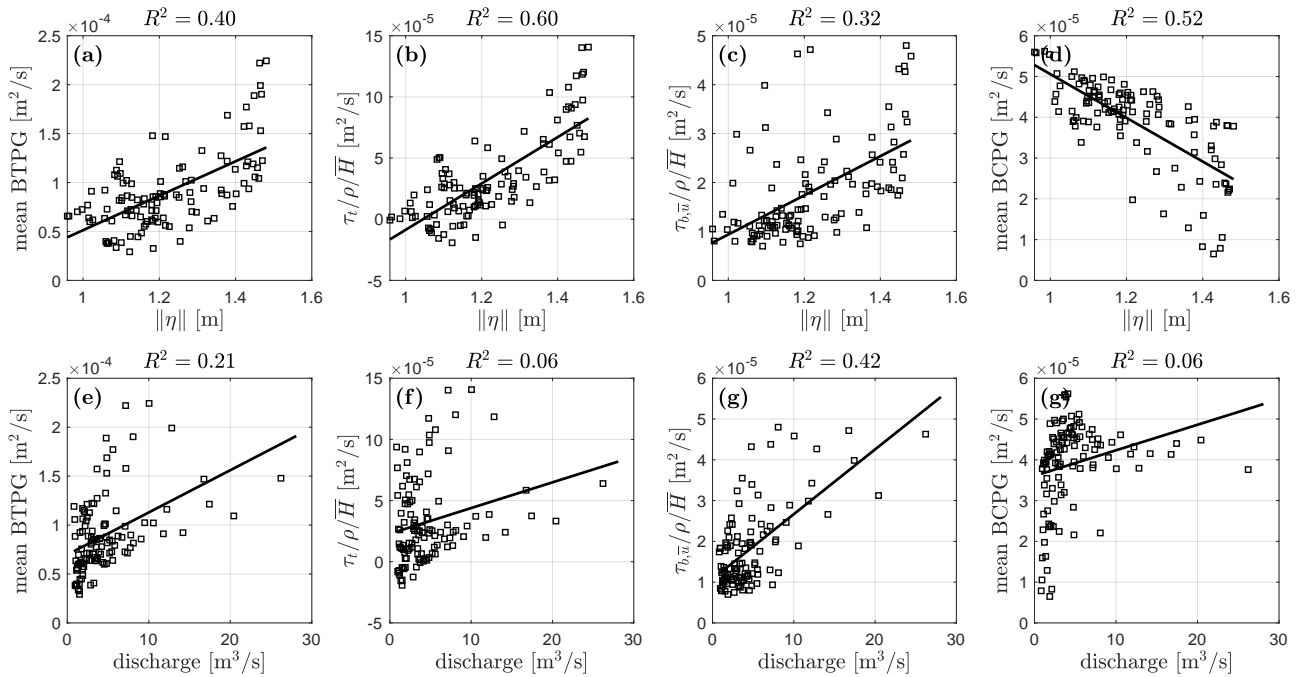


Figure A.1: Correlation between the mean BTPG,  $\tau_t$ ,  $\tau_{b,\bar{u}}$ , the mean BCPG, and tidal amplitude, river discharge.

625 **Acknowledgements** The authors thank Adrian Mikhail P. Garcia and Jay Sisson for field work assistance. The  
 626 research leading to these results was funded by NSF awards OCE-1634480 and OCE-1634481. Data supporting  
 627 this study are available online (at <https://doi.org/10.5281/zenodo.4540332>).

## 628 **References**

- 629 Arcement, G. J. and Schneider, V. R. (1989). Guide for selecting manning's roughness coefficients for natural  
630 channels and flood plains.
- 631 Blanckaert, K. (2010). Topographic steering, flow recirculation, velocity redistribution, and bed topography in  
632 sharp meander bends. *Water Resources Research*, 46(9).
- 633 Blanckaert, K. (2015). Flow separation at convex banks in open channels. *Journal Of Fluid Mechanics*, 779:432–  
634 467.
- 635 Blanckaert, K. and de Vriend, H. J. (2003). Nonlinear modeling of mean flow redistribution in curved open  
636 channels. *Water Resources Research*, 39(12).
- 637 Blanckaert, K. and Graf, W. H. (2004). Momentum transport in sharp open-channel bends. *Journal of Hydraulic  
638 Engineering*, 130(3):186–198.
- 639 Blanckaert, K., Kleinhans, M. G., McLelland, S. J., Uijtewaal, W. S., Murphy, B. J., van de Kruijs, A., Parsons,  
640 D. R., and Chen, Q. (2013). Flow separation at the inner (convex) and outer (concave) banks of constant-width  
641 and widening open-channel bends. *Earth Surface Processes and Landforms*, 38(7):696–716.
- 642 Bo, T. and Ralston, D. K. (2020). Flow separation and increased drag coefficient in estuarine channels with  
643 curvature. *Journal of Geophysical Research: Oceans*, page e2020JC016267.
- 644 Bowden, K. and Fairbairn, L. (1956). Measurements of turbulent fluctuations and reynolds stresses in a tidal current.  
645 *Proceedings of the Royal Society of London. Series A. Mathematical and Physical Sciences*, 237(1210):422–438.
- 646 Bricker, J. D., Inagaki, S., and Monismith, S. G. (2005). Bed drag coefficient variability under wind waves in a  
647 tidal estuary. *Journal of Hydraulic Engineering*, 131(6):497–508.
- 648 Chang, H. H. (1983). Energy expenditure in curved open channels. *Journal of Hydraulic Engineering*,  
649 109(7):1012–1022.
- 650 Chang, H. H. (1984). Variation of flow resistance through curved channels. *Journal of Hydraulic Engineering*,  
651 110(12):1772–1782.
- 652 Chant, R. J. (2002). Secondary circulation in a region of flow curvature: Relationship with tidal forcing and river  
653 discharge. *Journal of Geophysical Research: Oceans*, 107(C9):14–1.

654 Chow, V. T. (1959). Open-channel hydraulics. In *Open-channel hydraulics*. McGraw-Hill.

655 Dietrich, W. E. and Smith, J. D. (1983). Influence of the point bar on flow through curved channels. *Water*  
656 *Resources Research*, 19(5):1173–1192.

657 Dronkers, J. J. (1964). *Tidal computations in rivers and coastal waters*. North-holland publishing company Ams-  
658 terdam.

659 Ferguson, R. I., Parsons, D. R., Lane, S. N., and Hardy, R. J. (2003). Flow in meander bends with recirculation at  
660 the inner bank. *Water Resources Research*, 39(11):299–13.

661 Finotello, A., Ghinassi, M., Carniello, L., Belluco, E., Pivato, M., Tommasini, L., and D’Alpaos, A. (2020). Three-  
662 dimensional flow structures and morphodynamic evolution of microtidal meandering channels. *Water Resources*  
663 *Research*, 56(7):e2020WR027822.

664 Fong, D. A., Monismith, S. G., Stacey, M. T., and Burau, J. R. (2009). Turbulent stresses and secondary currents in  
665 a tidal-forced channel with significant curvature and asymmetric bed forms. *Journal of Hydraulic Engineering*,  
666 135(3):198–208.

667 Geyer, W. R. (1993). The importance of suppression of turbulence by stratification on the estuarine turbidity  
668 maximum. *Estuaries*, 16(1):113–125.

669 Geyer, W. R. (2010). Estuarine salinity structure and circulation. *Contemporary issues in estuarine physics*, pages  
670 12–26.

671 Geyer, W. R., Trowbridge, J. H., and Bowen, M. M. (2000). The dynamics of a partially mixed estuary. *Journal of*  
672 *Physical Oceanography*, 30(8):2035–2048.

673 Grant, W. D. and Madsen, O. S. (1982). Movable bed roughness in unsteady oscillatory flow. *Journal of Geophys-*  
674 *ical Research: Oceans*, 87(C1):469–481.

675 Grant, W. D. and Madsen, O. S. (1986). The continental-shelf bottom boundary layer. *Annual review of fluid*  
676 *mechanics*, 18(1):265–305.

677 Gross, E. S., Koseff, J. R., and Monismith, S. G. (1999). Three-dimensional salinity simulations of south san  
678 francisco bay. *Journal of Hydraulic Engineering*, 125(11):1199–1209.

679 Heathershaw, A. and Simpson, J. (1978). The sampling variability of the reynolds stress and its relation to boundary  
680 shear stress and drag coefficient measurements. *Estuarine and Coastal Marine Science*, 6(3):263–274.

681 James, C., Liu, W., and Myers, W. (2001). Conveyance of meandering channels with marginal vegetation. *Pro-*  
682 *ceedings of the Institution of Civil Engineers-Water and Maritime Engineering*, 148(2):97–106.

683 Jamieson, E. C., Ruta, M. A., Rennie, C. D., and Townsend, R. D. (2013). Monitoring stream barb performance in  
684 a semi-alluvial meandering channel: flow field dynamics and morphology. *Ecohydrology*, 6(4):611–626.

685 Kadlec, R. H. (1990). Overland flow in wetlands: vegetation resistance. *Journal of Hydraulic Engineering*,  
686 116(5):691–706.

687 Kaimal, J. C., Wyngaard, J., Izumi, Y., and Coté, O. (1972). Spectral characteristics of surface-layer turbulence.  
688 *Quarterly Journal of the Royal Meteorological Society*, 98(417):563–589.

689 Kalkwijk, J. P. T. and Booij, R. (1986). Adaptation of secondary flow in nearly-horizontal flow. *Journal of*  
690 *Hydraulic Research*, 24(1):19–37.

691 Kimball, P., Bailey, J., Das, S., Geyer, R., Harrison, T., Kunz, C., Manganini, K., Mankoff, K., Samuelson, K.,  
692 Sayre-McCord, T., et al. (2014). The whoi jetyak: An autonomous surface vehicle for oceanographic research  
693 in shallow or dangerous waters. In *2014 IEEE/OES Autonomous Underwater Vehicles (AUV)*, pages 1–7. IEEE.

694 Kranenburg, W. M., Geyer, W. R., Garcia, A. M. P., and Ralston, D. K. (2019). Reversed lateral circulation in a  
695 sharp estuarine bend with weak stratification. *Journal of Physical Oceanography*.

696 Lacy, J. R. and Monismith, S. G. (2001). Secondary currents in a curved, stratified, estuarine channel. *Journal of*  
697 *Geophysical Research: Oceans*, 106(C12):31283–31302.

698 Leeder, M. R. and Bridges, P. H. (1975). Flow separation in meander bends. *Nature*, 253:1–2.

699 Lentz, S. J., Davis, K. A., Churchill, J. H., and DeCarlo, T. M. (2017). Coral reef drag coefficients–water depth  
700 dependence. *Journal of Physical Oceanography*, 47(5):1061–1075.

701 Leopold, L. B. (1960). *Flow resistance in sinuous or irregular channels*. US Government Printing Office.

702 Leopold, L. B. and Wolman, M. G. (1960). River meanders. *Geological Society of America Bulletin*, 71(6):769–  
703 793.

704 Lewis, R. and Lewis, J. (1987). Shear stress variations in an estuary. *Estuarine, Coastal and Shelf Science*,  
705 25(6):621–635.

706 MacCready, P., Pawlak, G., Edwards, K., and McCabe, R. (2003). Form drag on ocean flows. In *Near Boundary*  
707 *Processes and Their Parameterization: Proc. 13th'Aha Huliko'a Hawaiian Winter Workshop*, pages 119–130.

708 Marani, M., Lanzoni, S., Zandolin, D., Seminara, G., and Rinaldo, A. (2002). Tidal meanders. *Water Resources*  
709 *Research*, 38(11):7–17–14.

710 Marriott, M. J. (1998). *Hydrodynamics of flow around bends in meandering and compound channels*. PhD thesis,  
711 University of Herfordshire.

712 McCabe, R. M., MacCready, P., and Pawlak, G. (2006). Form drag due to flow separation at a headland. *Journal*  
713 *of physical oceanography*, 36(11):2136–2152.

714 Monismith, S. G., Hirsh, H., Batista, N., Francis, H., Egan, G., and Dunbar, R. B. (2019). Flow and drag in a  
715 seagrass bed. *Journal of Geophysical Research: Oceans*, 124(3):2153–2163.

716 Nanson, R. A. (2010). Flow fields in tightly curving meander bends of low width-depth ratio. *Earth Surface*  
717 *Processes and Landforms: The Journal of the British Geomorphological Research Group*, 35(2):119–135.

718 Nepf, H. (1999). Drag, turbulence, and diffusion in flow through emergent vegetation. *Water resources research*,  
719 35(2):479–489.

720 Nidzieko, N. J., Hensch, J. L., and Monismith, S. G. (2009). Lateral Circulation in Well-Mixed and Stratified  
721 Estuarine Flows with Curvature. *Journal of Physical Oceanography*, 39(4):831–851.

722 Nihoul, J. C. and Roday, F. C. (1975). The influence of the “tidal stress” on the residual circulation. *Tellus*,  
723 27(5):484–490.

724 Parker, B. B. (2007). Tidal analysis and prediction.

725 Prandle, D. (1978). Residual flows and elevations in the southern north sea. *Proceedings of the Royal Society of*  
726 *London. A. Mathematical and Physical Sciences*, 359(1697):189–228.

727 Rogers, J. S., Maticka, S. A., Chirayath, V., Woodson, C. B., Alonso, J. J., and Monismith, S. G. (2018). Connecting  
728 flow over complex terrain to hydrodynamic roughness on a coral reef. *Journal of Physical Oceanography*,  
729 48(7):1567–1587.

730 Schnauder, I. and Sukhodolov, A. (2012). Flow in a tightly curving meander bend: effects of seasonal changes in  
731 aquatic macrophyte cover. *Earth Surface Processes and Landforms*, 37(11):1142–1157.

732 Seim, H., Blanton, J., and Elston, S. (2006). Tidal circulation and energy dissipation in a shallow, sinuous estuary.  
733 *Ocean Dynamics*, 56(3-4):360–375.

734 Seim, H. E., Blanton, J. O., and Gross, T. (2002). Direct stress measurements in a shallow, sinuous estuary.  
735 *Continental Shelf Research*, 22(11-13):1565–1578.

736 Seim, H. E. and Gregg, M. C. (1997). The importance of aspiration and channel curvature in producing strong  
737 vertical mixing over a sill. *Journal of Geophysical Research: Oceans*, 102(C2):3451–3472.

738 Signell, R. P. and Geyer, W. R. (1991). Transient eddy formation around headlands. *Journal of Geophysical*  
739 *Research: Oceans*, 96(C2):2561–2575.

740 Soulsby, R. (1990). Tidal current boundary layers, the sea, part 1. *Edited by: B. Le Méhauté, University of Miami,*  
741 *USA, John Wiley & Sons Inc., Printed in USA, ISBN: 0 471 63393 3.*

742 Soulsby, R. (1997). Dynamics of marine sands.

743 Sternberg, R. (1968). Friction factors in tidal channels with differing bed roughness. *Marine Geology*, 6(3):243–  
744 260.

745 Tennekes, H., Lumley, J. L., Lumley, J. L., et al. (1972). *A first course in turbulence*. MIT press.

746 Thomson, J. (1877). V. on the origin of windings of rivers in alluvial plains, with remarks on the flow of water  
747 round bends in pipes. *Proceedings of the Royal Society of London*, 25(171-178):5–8.

748 Trowbridge, J. H. and Lentz, S. J. (2018). The bottom boundary layer. *Annual Review of Marine Science*, 10:397–  
749 420.

750 Uncles, R. and Jordan, M. (1980). A one-dimensional representation of residual currents in the severn estuary and  
751 associated observations. *Estuarine and Coastal Marine Science*, 10(1):39–60.

752 van Rijn, L. C. (2011). Analytical and numerical analysis of tides and salinities in estuaries; part i: tidal wave  
753 propagation in convergent estuaries. *Ocean dynamics*, 61(11):1719–1741.

754 Vermeulen, B., Hoitink, A., and Labeur, R. (2015). Flow structure caused by a local cross-sectional area increase  
755 and curvature in a sharp river bend. *Journal of Geophysical Research: Earth Surface*, 120(9):1771–1783.

756 Walters, R. A. and Gartner, J. W. (1985). Subtidal sea level and current variations in the northern reach of san  
757 francisco bay. *Estuarine, Coastal and Shelf Science*, 21(1):17–32.

- 758 Zimmerman, J. (1978). Topographic generation of residual circulation by oscillatory (tidal) currents. *Geophysical*  
759 *& Astrophysical Fluid Dynamics*, 11(1):35–47.
- 760 Zimmerman, J. (1979). On the euler-lagrange transformation and the stokes' drift in the presence of oscillatory and  
761 residual currents. *Deep Sea Research Part A. Oceanographic Research Papers*, 26(5):505–520.